

FABRICATION AND
CHARACTERIZATION OF HIGH SPEED
RESONANT CAVITY ENHANCED
SCHOTTKY PHOTODIODES

A THESIS
SUBMITTED TO THE DEPARTMENT OF PHYSICS
AND THE INSTITUTE OF ENGINEERING AND SCIENCE
OF BILKENT UNIVERSITY
IN PARTIAL FULFILLMENT OF THE REQUIREMENTS
FOR THE DEGREE OF
MASTER OF SCIENCE

By
M. Saiful Islam
September 1996

TK
7871.89
.S35
I84
1996

**FABRICATION AND
CHARACTERIZATION OF HIGH SPEED
RESONANT CAVITY ENHANCED
SCHOTTKY PHOTODIODES**

A THESIS

SUBMITTED TO THE DEPARTMENT OF PHYSICS
AND THE INSTITUTE OF ENGINEERING AND SCIENCE
OF BILKENT UNIVERSITY
IN PARTIAL FULFILLMENT OF THE REQUIREMENTS
FOR THE DEGREE OF
MASTER OF SCIENCE

By

M. Saiful Islam

September 1996

TK

7871.80

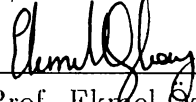
. S35

I84

1996

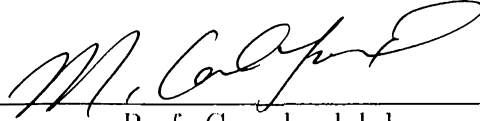
B. 01-236

I certify that I have read this thesis and that in my opinion it is fully adequate, in scope and in quality, as a dissertation for the degree of Master of Science.



Asst. Prof. Ekmel Özbay (Supervisor)

I certify that I have read this thesis and that in my opinion it is fully adequate, in scope and in quality, as a dissertation for the degree of Master of Science.




Prof. Cemal Yalabık

I certify that I have read this thesis and that in my opinion it is fully adequate, in scope and in quality, as a dissertation for the degree of Master of Science.



Asst. Prof. Orhan Aytür

Approved for the Institute of Engineering and Science:



Prof. Mehmet Baray,
Director of Institute of Engineering and Science

Abstract

FABRICATION AND CHARACTERIZATION OF HIGH SPEED RESONANT CAVITY ENHANCED SCHOTTKY PHOTODIODES

M. Saiful Islam

M. S. in Physics

Supervisor: Asst. Prof. Ekmel Özbay

September 1996

High speed, high external quantum efficiency and narrow spectral linewidth make resonant cavity enhanced (RCE) Schottky photodetector a good candidate for telecommunication applications. In this thesis, we present our work for the design, fabrication and characterization of a RCE Schottky photodiode with high quantum efficiency and high speed. We present experimental results on a RCE photodiode having an operating wavelength of 900 nm. The absorption takes place in a thin InGaAs layer placed inside the GaAs cavity. The active region was grown above a high-reflectivity GaAs/AlAs quarter-wavelength Bragg reflector. The top mirror consisted of a 200Å thin Au layer which also acted as Schottky metal of the device. An external quantum efficiency of 55% was obtained from our devices. We demonstrate that the spectral response can be tailored by etching the top surface of the microcavity. Our high speed measurements yielded a FWHM of 30 ps, which is the record response for any RCE Schottky photodiode ever reported.

Keywords: High Speed, Resonant Cavity, Photodetector, Schottky Diode, High Quantum Efficiency, Fabry-Perot Cavity, Resonant Detector, Schottky Diode Detector, Enhancement.

Özet

RESONANT BOŞLUK DESTEKLİ YÜKSEK HIZLI SCHOTTKY FOTODEDEKTÖRLERİNİN YAPIMI VE KARAKTERİZASYONU

M. Saiful Islam

Fizik Yüksek Lisans

Tez Yöneticisi: Asst. Prof. Ekmel Özbay

Eylül 1996

Yüksek hızı, yüksek verimi ve dar tayf aralığı ile, rezonant boşluk destekli (RCE) Schottky (Şotki) fotodedektörleri iletişim alanında çok önemli bir konuma gelmiştir. Bu tezde yüksek hızlı, yüksek verimli Schottky fotodedektörlerinin yapımı ve bu araçların özellikleri, karakterizasyon verileri sunulmaktadır. Deneysel sonuçlar 900 nanometre dalga boyunda çalışan RCE fotodiyotları ile elde edilmiştir. Soğurulma GaAs boşluğuna yerleştirilen ince bir InGaAs tabakasında gerçekleşmektedir. Aktif bölge, yüksek yansıtıcılığa sahip GaAs/AlAs çeyrek dalgaboyu Bragg aynaları üzerinde büyütülmüştür. Üst ayna 200Å kalınlığında ince bir altın tabakadan oluşmakta ve aygıtın Schottky metali olarak rol oynamaktadır. Mikroboşluğun üst yüzeyinin aşındırılmasıyla aracın tayf özellikleri değiştirilebilir. Yüksek hız ölçümlerimize göre, fotodedektörlerimiz 30 pikosaniyelik bir hıza sahiptir.

Anahtar

sözcükler: yüksek hız, rezonant boşluk, fotodedektör, Schottky diyot, yüksek kuvantum verimi, Fabry-Perot boşluğu, Resonant dedektör, Schottky diyot dedektörü

Acknowledgement

It is my pleasure to express my deepest gratitude to my supervisor Assist. Prof. Ekmel Özbay for his guidance, encouragement and invaluable efforts throughout my thesis works. I have not only benefited from his wide spectrum of interest in experimental physics but also learned a lot from his superior academic personality.

I would like to address my special thanks to Assist. Prof. Orhan Aytür for showing keen interest to establish the experimental setup for the characterization of the photodiodes, Assist. Prof M. Selim Ünlü for providing stimulating ideas and Prof. Atilla Aydınli for kindly helping us in some of our experimental works. Here I would also thank Mutlu Gökkavaş and Bora Onat who are the inseparable partners of this high speed photodetector project.

I thank all the ARL family especially Mr. İsmet İ. Kaya, Murat Güre, Erhan Ata, Talal Azfar and Erol Sağol for making a joyful environment and extending their helping hands whenever I needed. I owe thanks to Sanlı A. Ergun for all the patience he showed while teaching me the tedious job of bonding.

My sincere thanks are due to my parents for their moral support. Last but not least, I thank Hasina for her patience and making the life most joyful.

This project was supported by TÜBİTAK EEEAG-156.

Contents

Abstract	i
Özet	iii
Acknowledgement	iv
Contents	v
List of Figures	viii
1 Introduction	1
2 Theory of Operation	6
2.1 Schottky Junction as a Photodetector	7
2.2 Current-Voltage Characteristics	9
2.3 Quantum Efficiency	10
2.4 Transport of the Carriers	12
2.5 High Frequency Design	16
3 Fabrication Process	20
3.1 Process Description	21
3.1.1 Cleaning and Wafer Preparation	21
3.1.2 Photolithography	22
3.1.3 Wet Etching	23
3.1.4 Metalization	25

3.1.5	Annealing	26
3.1.6	RIE (Reactive Ion Etching)	26
3.1.7	PECVD (Plasma Enhanced Chemical Vapor Deposition)	27
3.1.8	Airbridge	28
3.2	Mask Design	29
3.3	Device Processing of Photodiodes	31
3.3.1	Ohmic Contact Formation	31
3.3.2	RTP (Rapid Thermal Processing)	32
3.3.3	Mesa Isolation	33
3.3.4	Interconnect metal	34
3.3.5	Schottky Metalization	34
3.3.6	Dielectric Deposition	35
3.3.7	Airbridge	36
4	Resonant Cavity Enhancement	38
4.1	Mechanism of Efficiency Enhancement with a Resonant Cavity	39
4.2	Scattering Matrices	41
4.3	The Components of the Resonant Cavity	46
4.3.1	The Bottom Reflector	47
4.3.2	The Top Mirror	48
4.4	Device Structure	48
4.5	Reflection Properties of MBE Structures	51
4.6	Anti-reflection Coating	52
4.7	Wavelength Tuning	53
5	Measurement and Results	55
5.1	Photospectrometric Analysis	56
5.1.1	Reflectivity Measurements	56
5.1.2	Photocurrent Measurements	61
5.2	I-V Characterization	66
5.3	Barrier Height Measurement	67
5.4	High Speed Measurements	68

List of Figures

2.1	Energy band-diagram of a metal-semiconductor junction.	7
2.2	Photogenerated carriers are swept away by the electric field.	9
2.3	The carriers generated at a depth W induces an output current during their transport across the depletion region.	12
2.4	The induced current waveform as a function of time.	14
2.5	Expected output waveform of a photodiode with a uniform density of photogenerated carriers.	15
2.6	Expected output waveform of a photodiode where the hole velocities are smaller than the electron velocities.	16
2.7	(a)Schematics of photodiode circuitry, (b) Equivalent circuit model for a high frequency analysis. (c) The scanned photograph is marked with conventional signs of circuit elements.	18
3.1	Two diode masks with differwent shape of active regions. The one on the left with bigger active area is used for photocurrent measurements and the one on the right with small active area is used for high speed measurements.	30
3.2	Test patterns of resitor and transmission line on the mask. The rectangular bar in between two square pads is the resistor. The numbers are the distances in microns between the transmission line test patterns.	31
3.3	Crosssection of a photodiode showing different components.	35
3.4	Photomicrographs of two different diodes. The active region of diode (a) is zoomed in figure (b). Figure (c) is a large area doide.	36

4.1	Analysis model of an RCE photodetector. The active region of thickness d is a small bandgap semiconductor. The top and bottom distributed Bragg reflection mirrors consist of alternating layers of non-absorbing larger bandgap materials.	39
4.2	Quantum efficiency of an RCE photodiode. The dashed straight line shows the maximum attainable quantum efficiency for a conventional photodetector of same thickness.	40
4.3	Changes of wave functions at the interface two media. For simplicity, a one-dimensional problem is assumed.	42
4.4	Schematic diagram of the wave function traveling through two sections of medium,	43
4.5	Simple optical layer without any interface	44
4.6	Optical layer with an interface.	45
4.7	Absorption layer in a stack.	46
4.8	Reflectivity of QWS for different numbers of stack pairs.	47
4.9	Epitaxial layer design of a top illuminated resonant cavity enhanced photodiode wafer. In bottom illuminated wafer, the InGaAs layer is 343 Angstrom. Number of pairs of GaAs/AlAs bottom mirror is 15 in the top and 10 in the bottom illuminated sample. The top mirror is Au layer which we deposit over the surface of the wafer during the fabrication.	49
4.10	SEM micrograph of the resonant microcavity and the bottom mirror.	50
4.11	Reflectivity with respect to the wavelength for RCE1 sample, the resonance is at 915 nm.	51
4.12	Reflectivity vs. wavelength for RCE2 sample, the resonance is at 940 nm.	52
4.13	The shifts of the resonance wavelength with cavity etching.	53
5.1	Experimental setup for measuring the reflectivity.	56
5.2	Reflectivity of a bare GaAs wafer.	57
5.3	Simulated and measured reflectivity of RCE1.	58
5.4	Simulated and measured reflectivity of RCE2.	58

5.5	Reflectivities of two RCE1 structures grown in two different MBE facilities. The peaks are 35nm apart from each other.	59
5.6	Measured reflectivity of 300Å etched RCE2 sample with the reflectivity of unetched RCE2. The resonance wavelength of the etched RCE2 is 925 nm while the original is 945 nm. The direction of wavelength shift is shown by an arrow.	59
5.7	Measured reflectivity of 600Å etched RCE2 sample and the unetched RCE2. The resonance of the etched RCE2 is 906 nm. The direction of wavelength shift is shown by an arrow.	60
5.8	Measured reflectivity of 900Å etched RCE2 sample and the unetched RCE2. The peak of the etched RCE2 moved to 892 nm. The direction of wavelength shift is shown by an arrow.	60
5.9	Photocurrent measurement setup.	61
5.10	Measured photocurrent from the RCE1 sample. The peak wavelength is 894nm.	62
5.11	Simulated quantum efficiency of RCE1 sample. The peak is at 896 nm.	62
5.12	Measured photocurrent from the RCE2 sample. The peak wavelength is 925 nm.	63
5.13	Simulated quantum efficiency of RCE2 sample. The peak is at 925nm.	63
5.14	Measured photocurrent from the RCE2 320Å etched sample. The peak wavelength is 900 nm.	64
5.15	Simulated quantum efficiency of RCE2 320Å etched sample. The peak is at 900 nm.	64
5.16	Quantum efficiency measurements of RCE1 diodes done at BU. The peak is at 900 nm.	65
5.17	I-V characteristics of a small area photodiode.	66
5.18	High speed measurement setup.	68
5.19	High speed measurement of an RCE2 diode with an area of $20\mu\text{m} \times 30\mu\text{m}$. At $\lambda = 850\text{nm}$, FWHM is 35 ps.	69

5.20	High speed measurement of an RCE2 diode with an area of $7\mu\text{m} \times 7\mu\text{m}$. At $\lambda = 850\text{ nm}$, FWHM is 35 ps.	70
5.21	High speed measurement of a 320\AA etched RCE2 diode with an area of $7\mu\text{m} \times 14\mu\text{m}$. At $\lambda = 900\text{ nm}$, FWHM is 45 ps.	70
5.22	High speed measurement of an RCE1 diode with an area of $20\mu\text{m} \times 30\mu\text{m}$. At $\lambda = 890\text{ nm}$, FWHM is 68 ps.	71
5.23	High speed measurement of an RCE2 diode with an area of $7\mu\text{m} \times 7\mu\text{m}$. At $\lambda = 900\text{ nm}$, FWHM is 30 ps.	72

Chapter 1

Introduction

The introduction of high speed devices to modern computer and telecommunication applications will result in enormous changes that are even hard to predict today. During the last two decades, we saw an unprecedented development in telecommunications, microelectronics and microcomputers. Our daily life and economic activities are already integrated with these new technologies on such a level that, scientific research and development on communication technologies is intensely pursued in all developed countries. This trend is expected to continue in the future and there will be need for more functional, faster and better devices to replace the existing ones.

Researchers have known the technical advantages of GaAs as compared to Si for decades. High mobility and high saturation drift velocity allow GaAs semiconductor devices to operate at microwave frequencies, where Si devices are unable to function effectively. GaAs can also be used as a semi-insulating substrate which provides lower interconnection capacitance and true monolithic circuit implementation. Furthermore, GaAs is a direct bandgap semiconductor. All of these properties make GaAs (and related materials) the ideal choice for high speed electronics and optoelectronics applications.

This thesis describes our work on ultrafast GaAs-based photodiodes which are important devices for applications in high-speed optoelectronics. High performance photodiodes with a very fast response and high sensitivity, are

becoming of increasing importance as the capacity of optical communication systems expand beyond multigigabit rates and the technology of optical receivers progresses towards total optoelectronic integration. The optical fiber has proven to be an ideal transmission medium with transmission capabilities that are theoretically four orders of magnitude higher than microwave communication systems. To exploit the maximum of this potential, light sources and detectors with very high bandwidths are necessary. Semiconductor-based light sources and detectors, with their fast electrical response and appropriate optical properties are currently used to achieve this purpose. We saw enormous developments in the area of light sources like lasers and LEDs, in a broad wavelength range from visible to the infrared spectrum. It became equally necessary to have a variety of high-performance photodetectors available for detection in the corresponding wavelengths of lasers and LEDs.

Research and development is actively pursued all over the world to attain photodiodes with low noise, high responsivity, large bandwidth, short response time and high gain-bandwidth. Photodetectors like p-n junction, PIN diode, avalanche photodiodes etc. are some of the depletion mode operational photodetectors widely used in photoreceivers. The reason behind the wide usage of depletion mode photodetectors is their low operational voltage, high sensitivity and high speed properties.

We have chosen to work on Schottky photodiodes because of their high speed properties. Although it is the simplest of all semiconductor devices, as it consist of a single semiconductor-metal junction, it offers excellent high frequency performance in a wide variety of applications. The Schottky diode is used in microwave mixers,¹ detectors,² and harmonic multiplier applications,³ at operating frequencies exceeding several THz. GaAs and InGaAs are the materials of choice to fabricate high speed detectors. Due to bandgap limitations, GaAs devices are sensitive only for wavelengths shorter than 890 nm. For longer wavelength high speed applications, InGaAs is the most suitable photoactive material. In 1983, S.Y. Wang and D. B. Bloom⁴ were the first to demonstrate a GaAs photodiode with a 3-dB bandwidth exceeding 100 GHz with a temporal

response of 4.5 ps. Later, in 1989, Parker et. al.⁵ succeeded in achieving up to 110 GHz performance. In 1991, Özbay et al.⁷ integrated an ultrafast GaAs Schottky photodiode with an all-electronic sampler and showed a temporal response of 1.8 ps corresponding to a 3-dB bandwidth of 200 GHz.⁸

For longer wavelength photodetection, Wey et al.¹¹ reported a InGaAs based photodiode with 3.8 ps FWHM corresponding to a band width of 70 GHz. In 1995, I-Hsing et al.⁶ fabricated a detector with a bandwidth of 120GHz. Despite their ultra high speeds, all these diodes were limited by very low quantum efficiency, all below 35%.

The absorption coefficient of the active layer material in a photodetector is typically around 10^4cm^{-1} . In order to ensure substantial absorption of the incident light and thus increase the sensitivity and quantum efficiency, the thickness of the active layer of conventional photodetectors has to be chosen accordingly. As an example, in order to achieve quantum efficiency greater than 80%, photodetectors with absorbing layer thicker than $1.8\mu\text{m}$ are needed. On the other hand, detectors with thin absorbing regions are of great interest for two reasons. First, a thinner absorption layer means shorter carrier transit time and hence, higher detector speed. Second, in optoelectronic integration, a thinner low band gap layer means greater structural compatibility with electronic devices, which would lead to many new design options.

An alternative strategy of enhancing the absorption is a newly developed idea of using a resonant structure.²³ In other words, a thin absorbing layer can be placed in a Fabry-Perot microcavity which is a resonator constructed of two parallel, highly reflective, flat mirrors separated by a certain distance. This microcavity enhances the performance of the devices by “recycling” of optical signals. Diode lasers were the first semiconductor devices to employ a resonant structure to enhance emission properties. The optical field is partially absorbed each time it crosses the thin absorbing layer, hence a multiple-pass absorption is obtained. The main advantage of the resonant detector is that the quantum efficiency is enhanced at the resonant wavelength due to the constructive interference of the incident light and suppressed everywhere else, hence making

it highly wavelength selective. There are also other advantages of resonant cavity enhanced (RCE) structures like reported reduction in leakage current due to a reduced thermal generation current¹⁰ and a relaxation of the requirement for low doping in the intrinsic region of diode-based detectors.¹²

In the following chapters, we show that the quantum efficiency of an optically thin detector can be improved considerably over a restricted spectral range by using a highly reflecting back mirror and a suitably designed front reflector. We designed and fabricated GaAs/AlAs resonant cavity enhanced Schottky photodetectors with thin InGaAs absorbing layers. Our experiments verified the enhancement of the quantum efficiency and the high speed performance of the fabricated devices.

Chapter 2 first reviews the theory of Schottky diode, its application as a photodetector and the current-voltage characteristics. We later examine the transport of carriers, high frequency design, and define the related terminologies of the photodetector. We also present the description of the designed mask which was used to fabricate the photodiodes. The epilayer of the samples and the diode structures are also given in this chapter.

Chapter 3 contains the detailed descriptions of the design and fabrication of the photodiodes. Standard processing equipment and techniques, optimizations of process parameters, development of new processes and some problems faced during the processes are presented.

In chapter 4, we present the mechanism of enhancing the detector performance by introducing a resonant cavity. We briefly discuss the S-matrix theory, the design of various mirrors and antireflection coating of the microcavity. We later compare the simulation of etched RCE structures with the experimental results.

Chapter 5 describes the characterization of fabricated photodiodes. We discuss the measurement techniques used for testing the spectral photoresponse of the fabricated diodes, and high speed properties of the RCE photodetectors. The I-V characteristics and its quality, detectivity of the diodes are also discussed in detail. We measured an external quantum efficiency of 55% from our devices at the resonance wavelength of 900 nm. The quantum efficiency measurements

clearly revealed the resonant nature of our design for the diodes. We measured a temporal response of 30 psec full width at half maximum (FWHM) corresponding to a 3-dB bandwidth of 14 GHz. This is the highest speed of a RCE Schottky photodiode ever reported. Our future plans, the existing trends in this research and some concluding remarks are presented in chapter 6.

Chapter 2

Theory of Operation

Semiconductor based photodetectors are designed either as photoconductive devices or photodiodes. Photoconductive devices operate by sensing the change in the conductivity of the material, which is a result of the photogenerated charge carriers. Photodiodes, on the other hand, operate by transporting the photogenerated carriers rapidly through the diode junction, by means of a strong electric field that is supported in the junction depletion layer (the space-charge region at the junction, where the carrier densities are depressed). Photodiodes are classified in terms of the junction types forming the diode ($p-n$, $p-i-n$, Schottky etc.). A $p-n$ photodiode is a $p-n$ junction operating at reverse bias mode. The reverse current of the diode increases when carriers are photogenerated in the depletion region. A $p-i-n$ photodiode is a $p-n$ junction, with an intrinsic (i) layer between the p and n layers. The absorption of photons outside of the depletion layer causes a slow diffusion of photogenerated carriers into the depletion layer. This effect decreases the speed of the device. In order to achieve high speed operation, a different device structure having no room for outside absorption of photons is more effective. In 1938, Schottky suggested that the rectifying behaviour could arise from a potential barrier created at the boundary between a semiconductor and a metal and it could be used for various purposes including photon detection.¹³ We will discuss this photodetection mechanism below.

2.1 Schottky Junction as a Photodetector

A Schottky barrier can be described as the two infinite half-planes of material, one a metal and the other a semiconductor brought into contact. When metal makes contact with a semiconductor junction, the Fermi levels of the two materials must be coincident to achieve thermal equilibrium. The energy band diagram of the resulting structure is shown in Figure 2.1.

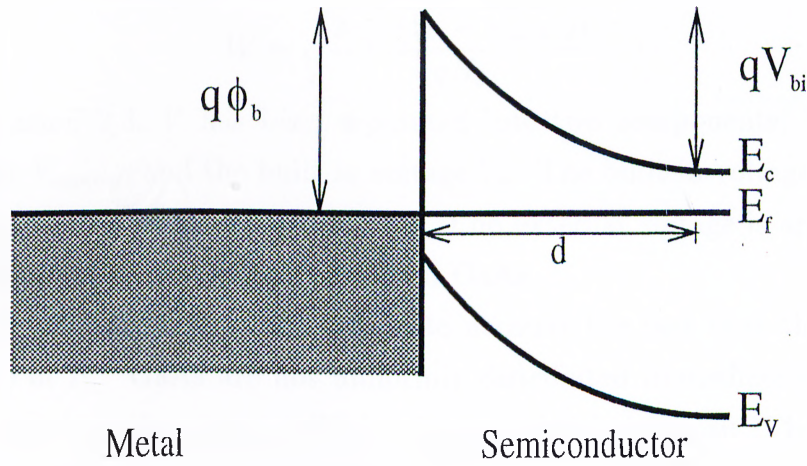


Figure 2.1: Energy band-diagram of a metal-semiconductor junction.

The work function of the metal Φ_m is the energy needed to remove an electron from the Fermi level E_f to the vacuum before contact. The work function of the semiconductor Φ_s is defined similarly and is a variable quantity which depends on the doping concentration. The difference between the two work functions, which is defined as contact potential Φ_b (Figure 2.1) acts as a potential barrier for the charged carriers. This results in a formation of a depletion region with a total voltage drop of V_{bi} across the region. The resulting two terminal device acts as a voltage rectifier and is called a Schottky diode.

By using Poisson's equation¹⁴ in the depletion region, we can obtain

$$V(x) = \left(\frac{qN_d}{\epsilon_0\epsilon_s}\right)\left(Wx - \frac{x^2}{2}\right) \quad (2.1)$$

where W is the width of the depletion region, x is the distance from the metal semiconductor interface, N_d is the doping concentration, ϵ_0 is the free space

permittivity, ϵ_s is the dielectric constant of the semiconductor and q is the charge of an electron. Thus, at $x = W$,

$$V(W) = \left(\frac{qN_d}{\epsilon_0\epsilon_s}\right)\frac{W^2}{2} \quad (2.2)$$

Rearranging Equation 2.1 yields the standard expression for the Schottky barrier depletion width:

$$W = \sqrt{\frac{2\epsilon_0\epsilon_s(V_{bi} - V_{applied})}{qN_d}} \quad (2.3)$$

In the Equation 2.3, V has been separated into two components, the applied gate voltage $V_{applied}$, and the built-in voltage V_{bi} . The built-in voltage represents the fact that a depletion zone exists even if no external voltage is applied. It is approximately 0.8 eV for metals placed on GaAs.

A more exact analysis would take into account the fact that the electrons for the case of N^- GaAs are not uniformly distributed immediately below the depletion zone boundary at $x = W$, but have a distribution tail. This gives rise to an extra term of kT/q in the equation:

$$W = \sqrt{\frac{2\epsilon_0\epsilon_s(V_{bi} - V_{applied} - kT/q)}{qN_d}} \quad (2.4)$$

At room temperature, $kT/q = 0.026$ eV and this additional term is usually ignored.

Figure 2.2 shows the photodetection mechanism of a Schottky diode. By applying sufficiently high bias voltages, the whole N^- region can be depleted, resulting in a continuous electric field across the region. The device can be used as a photodetector in this mode. When an optical input of wavelength λ is applied to the depletion region, electron hole pairs are generated. The carriers are swept away by the electric field: holes moving to the metal and electrons moving to the semiconductor. The transport of the charged carriers induces a output current, I_{out} , at the terminal of the device.

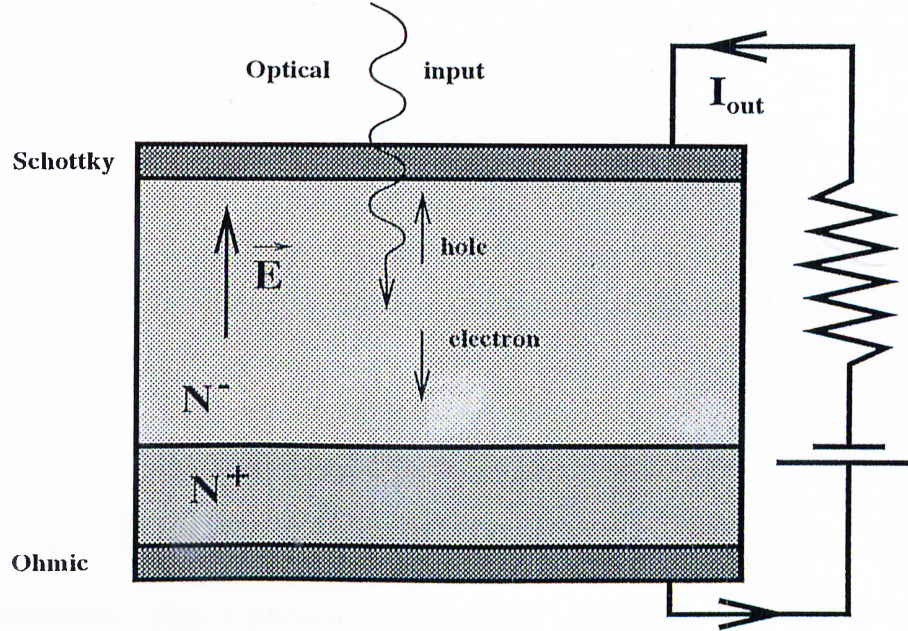


Figure 2.2: Photogenerated carriers are swept away by the electric field.

2.2 Current-Voltage Characteristics

In highly doped semiconductors ($N_d > 1.0 \times 10^{17} \text{ cm}^{-3}$) the Schottky barrier becomes so thin that electrons near the top of the barrier can tunnel through the barrier.¹⁵ This process is called *thermoionic-field emission*. In degenerate semiconductors with a small electron effective mass (such as GaAs), electrons can tunnel through the barrier near the Fermi level (field emission). The current voltage characteristic in case of the thermoionic field emission is determined by the competition between the thermal activation and tunneling and is given by,

$$\begin{aligned} J &= A^* T^2 \exp(-q\phi_b/kT) [\exp(qV/kT) - 1] \\ &= J_s [\exp(qV/kT) - 1] \end{aligned} \quad (2.5)$$

where $J_s = A^* T^2 \exp(-q\phi_b/kT)$, $A^* = 4\pi m_e q K_B^2 / h^3$ is the effective Richardson constant, ϕ_b is the barrier height and m_e is the effective electron mass. For $V \gg kT/q$, we can write the Equation 2.5 as

$$J = J_s \exp(qV/kT) \quad (2.6)$$

Actual measurements of the current density usually fit the expression

$$J = J_s \exp(qV/nkT) \quad (2.7)$$

where n is the *ideality factor* and represents departure from an ideal Schottky junction ($n=1$). We will use Equation 2.7 to calculate the barrier height of the Schottky diodes in chapter 5. In terms of current, Equation 2.7 is

$$I = I_o \exp\left(\frac{qV}{nKT}\right) \quad (2.8)$$

2.3 Quantum Efficiency

The probability that a photon will generate an electron hole pair is defined as the *quantum efficiency*, which can be expressed as

$$\eta = \frac{I_p}{\frac{q}{h\nu} P_{opt}} \quad (2.9)$$

where I_p is the current photo generated by the absorption of incident field, P_{opt} is the incident optical power, h is Planck's constant, ν is the frequency of the incident light and q is the electronic charge. The quantum efficiency η is defined as the probability that a single photon incident on the photodiode will induce current in the external circuit. Quantum efficiency depends both on the optical and electronic properties of the semiconductor material and the physical structure of the device. Depending on materials, wavelength, and physical structure, only a portion of the incident optical power is absorbed in the depletion region. The remaining portion is reflected, transmitted, or absorbed in lossy regions such as the Schottky metal. The quantum efficiency is experimentally measured by the ratio of the absorbed optical power contributing to photocurrent to the incident optical power. Since the number of detected electrons is equal to the number of absorbed photons (neglecting recombination), quantum efficiency may also expressed as,

$$\eta = \text{Number of detected electrons} / \text{Number of incident photons.}$$

For a typical photodetector, the quantum efficiency is given by,

$$\eta = (1 - R_s)(1 - e^{-\alpha d}) \quad (2.10)$$

where R_s is the surface reflectivity, α is the power absorption coefficient and d is the thickness of the active detector material. In Equation 2.10, the first term represents the power that penetrates through the front surface of the photodiode while the second term represents the portion of the power that is absorbed along a layer of width d . From the Equation 2.10, it is observed that η can be increased by decreasing R and increasing d . The front surface reflectivity, R can be minimized using a dielectric coating as will be discussed in the next section. However, as was discussed in previous section, d can not be increased without increasing the transit-time.

Another important figure of merit is the *responsivity*, R , which is defined as the ratio of photocurrent to the incident optical power.

$$R = \frac{I_p}{P_{opt}} = \frac{\eta q}{h\nu} = \frac{\eta \lambda (\mu m)}{1.24} (A/W) \quad (2.11)$$

It is clear that the responsivity increases linearly with wavelength for a given quantum efficiency. Under the assumption that for each incident photon an electron-hole pair is generated and collected which means the quantum efficiency $\eta = 1$, the above expression can be written as

$$R = \frac{\lambda (\mu m)}{1.24} (A/W) \quad (2.12)$$

The *spectral response* of a photodiode is determined in the wavelength range in which an appreciable photocurrent can be measured. The key physical parameter which affects the spectral response is the optical absorption coefficient, α of the semiconductor from which the photodetector is fabricated.¹⁶ The short-wavelength limit of a photodetector is set by the wavelength in which the absorption coefficient of the semiconductor is in excess of 10^5 cm^{-1} . For wavelengths shorter than this value, the absorption of the photons takes place mostly near the surface. Thus for detectors with large surface recombination

velocity, the photocurrent produced by short-wavelength photons can be greatly reduced.

2.4 Transport of the Carriers

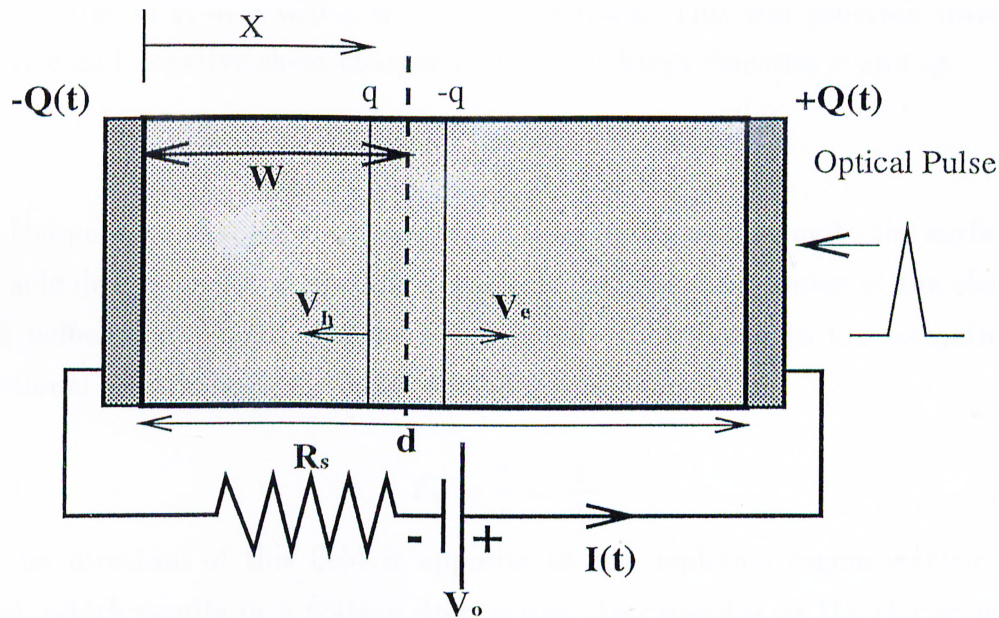


Figure 2.3: The carriers generated at a depth W induces an output current during their transport across the depletion region.

We can describe the transport of carriers and calculate the resulting current pulse by using the diagram in Figure 2.3. The depletion region can be described as a parallel plate capacitor, C , which is defined as

$$C = \frac{\epsilon A}{d} \quad (2.13)$$

where ϵ is the dielectric constant, A is the diode area and d is the depletion width. At steady state, the voltage bias on the capacitor is V_0 , which results in a steady state total charge of Q_0 across the capacitor.

$$Q_0 = CV_0 \quad (2.14)$$

The electric field E , across the depletion region is position dependent which can be expressed in terms of bias voltage as

$$V_0 = \int_0^d E(x) dx \quad (2.15)$$

Now suppose that, at $t = 0$, a narrow optical pulse generates carriers with a total charge of q , at a depth W from the surface. This will generate travelling positive and negative sheet charges with sheet charge densities σ and $-\sigma$.

$$\sigma = \frac{q}{A} \quad (2.16)$$

The positive charged sheet corresponds to the holes moving to the surface at the hole drift velocity, v_h and the negatively charged sheet moves at the electron drift velocity, v_e . Each charged sheet equally contributes to the formation of additional electric field, E_σ , between the sheets.

$$E_\sigma = \frac{\sigma}{\epsilon} = \frac{q}{A\epsilon} \quad (2.17)$$

The direction of this field is opposite to the depletion region electric field $E(x)$, which results in a voltage drop across the capacitor as the charge moves away. This voltage drop can be expressed as

$$V_\sigma(t) = \int_{x_h}^{x_e} E_\sigma dx = E_\sigma [x_e(t) - x_h(t)] \quad (2.18)$$

where $x_e(t)$ and $x_h(t)$ are the time dependent coordinates of the negative and positive charge sheet. These time dependent coordinates can be expressed as,

$$x_e(t) = W + v_e t \quad \text{for } 0 < t < t_e \quad (2.19)$$

$$x_h(t) = W - v_h t \quad \text{for } 0 < t < t_h \quad (2.20)$$

where the electron transit time, $t_e = \frac{d-W}{v_e}$, and hole transit time, $t_h = \frac{W}{v_h}$ are defined as the times required for each carrier to complete its transport. Assuming $t_e > t_h$ and using the Equations 2.19 and 2.20 we can write the time dependent voltage drop as,

$$V_{\sigma}(t) = \begin{cases} \frac{q}{A\epsilon}(v_e + v_h)t & \text{for } 0 < t < t_h \\ \frac{q}{A\epsilon}v_e t & \text{for } t_h < t < t_e \end{cases} \quad (2.21)$$

We can write the current $I_{out}(t)$ as,

$$I_{out}(t) = \frac{dQ(t)}{dt} = \frac{d}{dt}[CV(t)] \quad (2.22)$$

$$V(t) = V_0 - V_{\sigma}(t) \quad (2.23)$$

$$I_{out}(t) = \begin{cases} I_1 = \frac{q}{d}(v_e + v_h) & \text{for } 0 < t < t_h \\ I_2 = \frac{q}{d}v_e & \text{for } t_h < t < t_e \end{cases} \quad (2.24)$$

This time dependent expression is plotted in Figure 2.4. The total charge under the curve can be found by integrating $I_{out}(t)$,

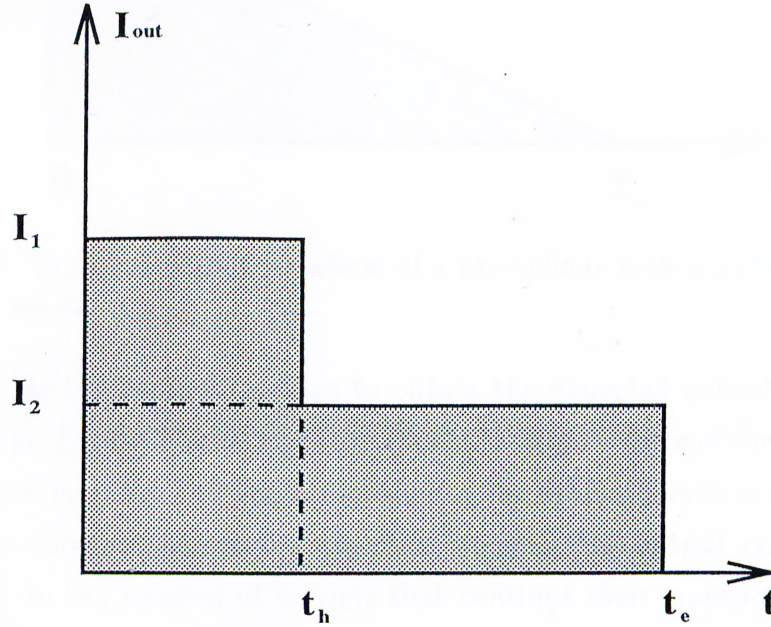


Figure 2.4: The induced current waveform as a function of time.

$$\Delta Q = \int_0^{t_e} I_{out}(t)dt = \frac{q}{d}V_e t_e + \frac{q}{d}V_h t_h = \frac{q}{d}V_e \left(\frac{d-W}{V_e}\right) + \frac{q}{d}V_h \left(\frac{W}{V_h}\right) = q \quad (2.25)$$

Thus, as expected from the conservation, an amount of charge generates a current such that the same amount of charge accumulates on the capacitor. Once all the carriers reach to the parallel plates, they recombine with these excess charge and steady state is reached.

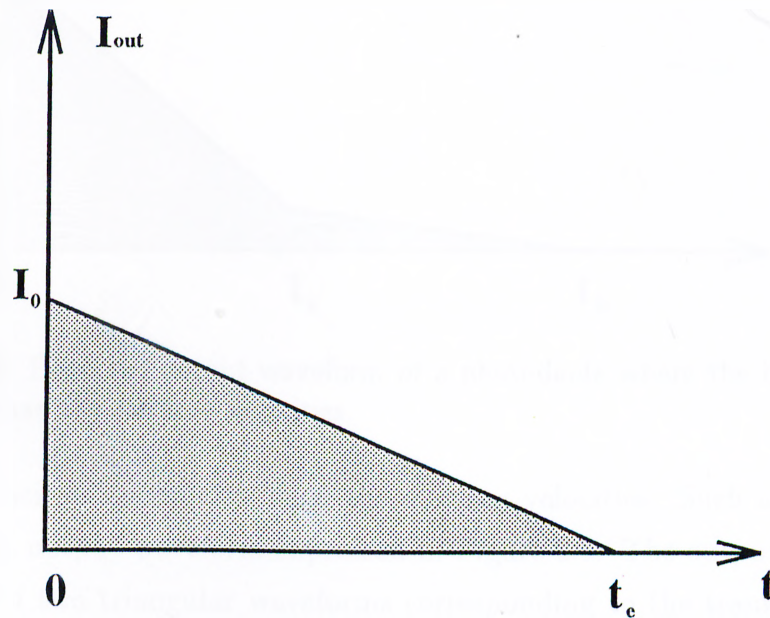


Figure 2.5: Expected output waveform of a photodiode with a uniform density of photogenerated carriers.

We can use the same formalism to obtain the expected output currents for different areas. Figure 2.5 describes the expected output of one of these situations. Let us assume $v_e = v_h$, and the absorption of the optical power is small enough that it stays constant across the depletion region. The output current will be proportional to the number of carriers that continue their transport. At $t = 0$, the number of carriers that induce the output current is maximum, so that output reaches its maximum at that time. But as the carriers closest to the metal and the other end of the depletion region completes their transport, the number of carriers continuing their transport decreases at a linear rate. This results in a linear drop in the induced current, giving the triangular waveform shown in Figure 2.5.

The assumption, $v_e = v_h$, does not hold for most of the semiconductors where

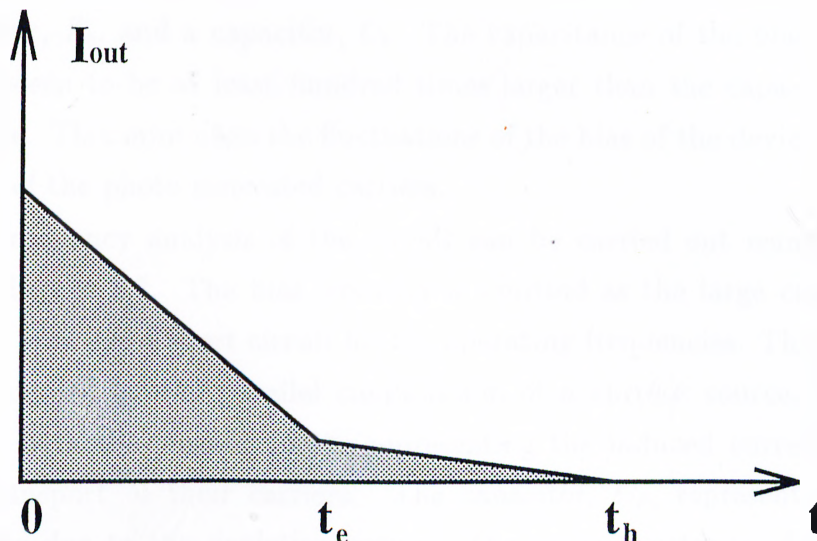


Figure 2.6: Expected output waveform of a photodiode where the hole velocities are smaller than the electron velocities.

the hole velocities are smaller than the electron velocities. Such a case results in a different output waveform expressed in Figure 2.6. The output is made up of the sum of two triangular waveforms corresponding to the transport of each carrier. The electron transport time $t_e = \frac{W}{v_e}$, is shorter than the hole transit time, $t_h = \frac{w}{v_h}$, and a tail is observed at the output waveform. This is due to the transport of the holes which are generated at the very end of the depletion region, and travel across the depletion region before reaching and recombining at the Schottky metal interface.

2.5 High Frequency Design

The speed of a photodetector is typically limited by three key factors, namely, the carrier diffusion time in the bulk quasi-neutral region, the carrier drift transit time across the depletion layer, and the RC time constant of the photodiode circuitry.¹⁷

The typical circuit configuration of a photodiode circuit is shown in Figure 2.7. A bias voltage is applied to the diode through a bias circuitry which consists

of a resistor, R_b , and a capacitor, C_b . The capacitance of the bias capacitor is usually chosen to be at least hundred times larger than the capacitance of the photodiode. This minimizes the fluctuations of the bias of the devices during the transport of the photo generated carriers.

High frequency analysis of the circuit can be carried out using the circuit model in Figure 2.7. The bias circuitry is omitted as the large capacitance of the device acts like a short circuit for the operating frequencies. The photodiode can be modeled by the parallel combination of a current source, $I_p(t)$ and a capacitor, with the current source representing the induced current generated by the transport of their carriers. The capacitor, C_d , represents the device capacitance due to the depletion region. The series resistance of the diode is much smaller than the load impedance, R_L , and is not included in the circuit model.

In the previous section, we calculated the expected induced current waveforms due to transport of the carriers in the depletion region. As explained before, our devices have very high absorption coefficients and have an induced waveforms very similar to the one shown in the Figure 2.4. This wavefunction can be mathematically described as a rectangular function,

$$I_p(t) = \begin{cases} I_1 & 0 < t < t_e \\ 0 & t_e < t \end{cases} \quad (2.26)$$

where I_1 is the magnitude of the induced current and t_e is the electron transit time, $t_e = \frac{d}{v_e}$. This can be expressed in the frequency domain as,

$$|I_p(\omega)| = I_1 \frac{\sin\left(\frac{\omega t_e}{2}\right)}{\frac{\omega t_e}{2}} \quad (2.27)$$

where the 3-dB roll-off frequency is given as,

$$f_{t_e}^{3-dB} = \frac{0.442}{t_e} = 0.442\left(\frac{v_e}{d}\right) \quad (2.28)$$

Using Figure 2.7, the frequency dependence of the output voltage can be expressed as,

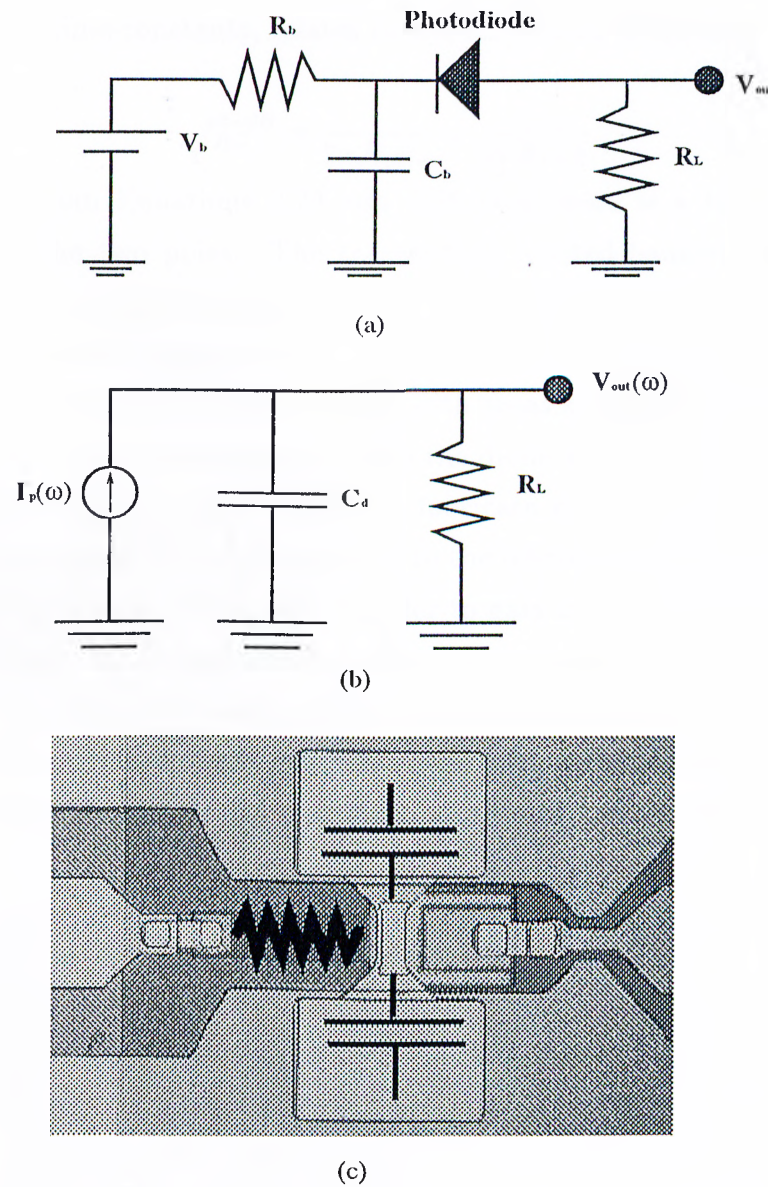


Figure 2.7: (a) Schematics of photodiode circuitry, (b) Equivalent circuit model for a high frequency analysis. (c) The scanned photograph is marked with conventional signs of circuit elements.

$$V_{out}(\omega) = I_p(\omega) \left(\frac{R_L}{1 + j\omega R_L C_d} \right) \quad (2.29)$$

This function has two poles. The first pole relates to equation $f_{t_e}^{3-dB} = \frac{0.442}{t_e} = 0.442 \left(\frac{v_e}{d} \right)$ which represents the transit time of the electrons, and the second pole,

due to the RC time constants, relates to the RC roll-off frequency

$$f_{RC}^{3-dB} = \frac{1}{2\pi R_1 C_d} = \frac{1}{2\pi R_1 \epsilon A} \quad (2.30)$$

It is seen from Equations 2.29 and 2.30 that there is a trade-off between the effects of the two poles. The transit-time limited bandwidth is inversely proportional to the depletion layer width d whereas the RC time-constant limited bandwidth is directly proportional d . To overcome this limitation, the area of the diode can be decreased. However, diodes with areas smaller than $10 \mu\text{m}^2$ are not feasible, because of several reasons. When the diode area decreases to such small sizes, it becomes increasingly difficult to fabricate it successfully. The airposts fabricated to connect the Schottky metal to the interconnect metal in the diodes occupy an area of at least $5 \times 5 \mu\text{m}^2$ in order to gain considerable durability. In a small area diode, the airposts cover most of the active region, leaving no room for incoming photons. Moreover, focusing of the optical beam becomes difficult and the series resistance of the diode increases with decreasing area. As a result, there is a practical limit for the maximum speed that can be attained from these devices.

Chapter 3

Fabrication Process

The fabrication of photodetectors involves many steps, each of which must be optimized to achieve acceptable performance with reliable and repeatable manufacturing yields. Out of seven steps of the process described in this chapter, two are completely new steps for our microfabrication laboratory. These are airpost and airbridge processes which were introduced to reduce parasitic capacitance of the devices. Thick metal evaporation was needed for a sustainable bridge, so we had to develop a new process for thick metal lift off. Critical steps like submicron alignment, repeated deposition of various metals, alloying, lift-off etc. needed considerable amount of process development time before we could start processing real devices. Subsequent sections of this chapter are concerned with specific stages followed in the fabrication of resonant cavity enhanced Schottky photodetectors. We first give an overall view of the standard semiconductor processes related to the fabrication of a photodiode and then at the end discuss our methods and experiences.

3.1 Process Description

3.1.1 Cleaning and Wafer Preparation

Due to the cost and difficulty of processing a whole wafer, we cleaved the wafer into small pieces. A diamond tipped scribing tool is used to mark along a crystalline direction lying within the surface plane. 0.8cm×0.8cm square shaped samples were processed with a mask of 0.5cm×0.5cm. Chemical cleaning procedure before lithography or after any process was observed strictly to ensure the best performance. First, samples were immersed in boiling Trichloroethane (TCE) bath for 2 minutes. Second, the samples are kept in a bath of room temperature acetone for five minutes. It was found that cleaning the sample surface with a clean cotton tipped tool worked quite well to clean out all residual materials or dirt. This mechanical brushing technique is very effective in removing particles contaminants by overcoming the adhesion forces. In the third step, the samples are dipped in boiling isopropanol for two minutes. At the end samples were left in flowing DI (deionized) water for two minutes before they were dried under continuous nitrogen gas flow. This was followed by a 120°C hot plate bake. This is known as dehydration baking which helps to improve adhesion of resist.

The cleaning processes are done under the precaution of not allowing the wafer to become dry before going to a subsequent rinsing. Otherwise, the evaporation of one of the solvents would leave behind residues that may not be soluble in the subsequent solvent. It is known that when the clean samples of GaAs are left in the open air, an oxide layer as thick as 30Å grows in four days. Furthermore, a carbon overlayer is also formed when steady state is reached. These layers may cause contact problems in the metalization step which was performed several times during the process of photodetector. It was found that etching the sample in a weak HF resulted in a very good contact in the metalization process.

3.1.2 Photolithography

Photolithography is the process of transferring patterns of geometric shapes on a photomask to a thin layer of radiation-sensitive material (photoresist) which covers the surface of a semiconductor wafer. These patterns define the various regions in an integrated circuit such as ohmic contacts, Schottky metals, mesa isolations, capacitors etc. The exposure is commonly accomplished by using UV light although electron beams, X-ray etc. can also be used. There are a number of photolithography techniques namely contact printing, proximity printing, projection printing, and optical stepping. Contact printing is the most popular in GaAs device fabrication. In this technique a mask is aligned on the wafer and then vacuum clamped directly against the wafer for exposure. A nearly collimated beam of ultraviolet light exposes the resist through the back of the mask for a fixed time. The contact between the mask and the resist provides very high resolution although there is a risk of damaging the mask from the abrasion during the printout operation. In our process contact printing was done by a Karl Suss MJS3 mask aligner at 365nm.

The photoresist used in our process is AZ5214E which is produced by Hoechst Celanese. This is a positive resist with high resolution, high sensitivity and excellent process latitude. Its spectral absorption peak is around 360nm which is ideally fit for Hg i-line (365nm) photolithography.

Process Data

After coating the samples with photoresist the samples were usually spun at 4000 rpm for 40 sec to have a resist thickness of 1.5 microns. In one process (airbridge) a thicker resist is needed. For that purpose, the sample were spinned at 2500 rpm which resulted in a 1.9 micron resist thickness. To improve adhesion 100% HMDS was applied at the same spin rate. Following the resist application, samples are soft baked at 110°C for 50 seconds over a hot plate to remove the water and solvents that remain in the film after spin-on.¹⁹ Samples are then exposed under UV-lamp at 345nm for 35 sec. The optical power per unit area is

measured to be $7.5\text{mW}/\text{cm}^2$, so the total dose is $262\text{ mJoule}/\text{cm}^2$. Developing step is completed in one minute in AZ312 MIF Developer (Developer : $\text{H}_2\text{O} = 1 : 1$). Samples are then rinsed in DI water to remove photoresist residues or scums. Finally samples are dried by N_2 gun gas flow. The resolution patterns of the masks and the quality of the photolithography is investigated using an optical microscope. If the resolution patterns are of good qualities, subsequent process steps are followed.

Chlorobenzene Application

When a thick metal deposition process follows a photolithography process, it is important to generate resist with overhanging edges. Metal deposition from some point source will then result in a film which is discontinuous over resist edges. Dissolution of the resist in acetone or resist thinner will then remove all metal over the resist, leaving only metal that was deposited on the semiconductor substrate. To attain such edges we did two things: we hardened the surface of the resist with chlorobenzene and we softened the underlying resist by incomplete softbaking. Although we consider that resist will not develop in areas where it has not been exposed, all practical resist have some small development rate even if unexposed. By under-baking the resist during softbake, unexposed development rate is increased in the depth of the resist whereas the resist surface is made harder with the help of chlorobenzene (CB). The edges of the resist then has a overhanging lip and a recessed side wall, whose slope is vertically outward. 15 minutes soak in CB is enough to harden $0.2\ \mu\text{m}$ of the upper surface of the resist. We used CB in the lithography process of interconnect and airbridge metalizations.

3.1.3 Wet Etching

After the patterns are defined using photoresist layer over the surface of the sample, the geometry is transformed onto underlying semiconducting structure by means of etching. A post bake at 120°C for 50 sec on the hot plate causes

the resist to adhere to the sample perfectly and results in an anisotropic etching. It was found that wet etches prefer etching based on crystallographic orientation with the (111) GaAs face, generally etching a factor of 2 to 5 times slower than the (100), (110) or (101) faces. In the photodiode process, wet etching was used to form mesa structure for device isolation, and to deposit ohmic metal on to the top of n^+ region which is embedded inside the wafer structure.

The mechanism is first to oxidize the surface with an oxidizing agent like hydrogen peroxide (H_2O_2), this is followed by removing the oxide (Ga_2O , Ga_2O_3 , As_2O_3 , As_2O_5 etc.) with the help of an acid or a base, thereby removing some of the Ga and As atoms.¹⁸ Initially, we tried ammonium hydroxide (NH_4OH) and hydrogen peroxide (H_2O_2) etchant with a ratio of 20 : 7 and 300 of H_2O . It was found that for 1 μm of vertical etch, around 2 μm of lateral etch was caused by this etchant. Later we tried sulfuric acidic etchant which showed equal lateral and vertical etch rates.²⁰ The ratio was $H_2SO_4 : H_2O_2 : H_2O = 1:8:80$ and etch rate was around 75 $\text{\AA}/\text{sec}$ for GaAs and 50 $\text{\AA}/\text{sec}$ for $In_{0.08}Ga_{0.92}As$ which was the photoactive material of our wafer structure.²¹

In designing the resistors and other components of the photodetector circuit, the undercut ratio was taken into consideration. Large fluctuations in the undercut could change the magnitude of resistance of the circuit resistors which could contribute negatively to the high speed measurements. Likewise, while etching the samples for ohmic metalization, large undercut could cause harm to the photodiodes. So the distance between the ohmic and Schottky metal in the mask was determined after the calculation of the probable undercut.

In order to ensure uniform rate of etching all over the sample, the RIE was used with O_2 plasma to clean the sample surfaces by ashing the residual photoresist over the exposed areas of the sample after the photolithography and post bake. Without RIE ashing, it was found that the chemical etch shows considerable fluctuations in the etch rate even at two nearby points. Again, while etching an RCE sample which has various types of materials embedded in it, it is always necessary to check the depth of etch very frequently as the rate varies from layer to layer. In the samples with resonant cavity, etching had to be very sensitive

because of the presence of a layer of AlAs directly under the insulating GaAs layer. Lack of caution in stopping the etching at the insulating GaAs layer might expose the AlAs which oxidizes within some nanoseconds, and may cause permanent adherence problem in the whole sample in the subsequent metalization processes.

3.1.4 Metalization

Metalization on GaAs serves many purposes like ohmic contacts, Schottky barrier, interconnect metal and airbridge formation. In our metalization processes, Leybold LE-560 box coater was used in which tungsten boats are used for thermal evaporation. This process is based on heating the source material to the temperature of vaporization in a high vacuum atmosphere and then deposit the vapor onto the sample surface. Evaporations were done in the region of 10^{-6} mbar and the distance between the boat and the sample was around 20 cm. As the amount of material evaporating from the boat reaching to distance d is given by the cosine of the axial angle times the main axis (axis perpendicular to the boat) of evaporation, samples were placed just on the top of the boat. Evaporation rate and melting point depend on two different parameters for Ti and Ni. One is the amount of material in the boat which acts as a thermal sink and the other is the current driven to the boat resistance. Using Ni and Ti powder, the evaporation energy was reduced to a considerable level although there is a risk of quality degradation because of oxidation over the surface of the metal powder. Despite 25 to 30 minutes are enough to reach the intended vacuum level, best results were obtained when the vacuum was applied for more than 45 minutes. Following chart gives relevant information of the metals we used in our processes.¹⁸

<i>Material</i>	<i>MeltingPoint(°C)</i>	<i>Densityg/cm</i>	<i>Resistivity10⁻⁶-cm</i>
<i>Ge(Germanium)</i>	937	5.3	—
<i>Au(Gold)</i>	1062	19.3	2.2
<i>Ni(Nickel)</i>	1453	8.9	7.0
<i>Ti(Titanium)</i>	1675	4.5	42.7

3.1.5 Annealing

Annealing is a thermal process in which a sample is heated to temperatures of 400 to 1400°C depending on the desired process after ohmic metalization is done. Our annealing was done in an AG-610 minipulse RTP device. RTP device was first purged with argon (Ar₂) for about three minutes to make the chamber free of water vapor. Samples are then put onto the Si wafer carriage and then heated with the radiation of a flash-lamp. In the n-type ohmic contact, GeAuNi metal layers are heated until they alloy into GaAs. With the rise of temperature, the AuGe alloy begins to melt and Ga diffuses into the metal. On the other hand, Ge diffuses into the wafer and acts as a dopant. Ge is an amphoteric dopant of GaAs and thus it should come to rest on the Ga sites of the crystal in quantities sufficient to dope the GaAs near $2 \times 10^{19} \text{ cm}^{-3}$.

3.1.6 RIE (Reactive Ion Etching)

In order to clean the sample surface before wet etching and to thin the resist layer of airpost step, RIE was used with the O₂ plasma. The machine was a parallel plate Leybold LE-301 reactive ion etcher operating at 13.56 MHz RF voltage. The chamber pressure can be lowered by turbo pumping down to few millibars. After the post bake at 120° C for 50 seconds, the resist was etched for about 2 minutes in the O₂ plasma under the following condition.

Gas flow : 20 sccm.

Pressure : Power

RF : 51 W

Self bias voltage = 322Volts

Etching Time : 120 sec

Total etched resist : 0.2 micron.

Without the application of RIE, the wet etching was found to show nonuniformity in etch rates from region to region on the same sample. In the formation of airposts, RIE gives better yields because of two reasons. First, Thinning a resist by O_2 plasma helps to remove the vulnerably soft and dissolvable upper layer of the resist which is essential for doing a better airpost step. Second, the residual resist over the exposed area of the samples is removed completely when thinning of resist takes place.

We previously tried RIE for etching Si_3N_4 films. It was found that RIE somehow caused damages to the dielectric layers by making cracks and reducing adhesive property. The gas for this etch was CHF_3 . Later we tried wet etching using dilute hydrofluoric acid (HF), with a ratio of $HF:H_2O=1:200$ and observed high performance.

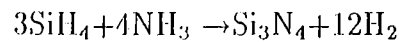
3.1.7 PECVD (Plasma Enhanced Chemical Vapor Deposition)

Silicon nitride is commonly used as a dielectric film and an antireflection coating in contemporary photonics and semiconductor industry. Among many other methods of film deposition, PECVD (Plasma Enhanced Chemical Vapor Deposition) is widely used since it enables low temperature deposition, controllable index of refraction and film stress as well as uniform film thickness and properties. Because of low temperature deposition, dopant redistribution minimization and protection of sensitive substrates can be achieved. Again PECVD allows us to control film stress and thus avoid cracking and poor adhesion problem.

In the fabrication of a photodiode, Si_3N_4 was deposited to act as a dielectric slab in between two plates of the circuit capacitors and an antireflection coating. The machine used for this purpose was a Plasma Technologies μp -Dp80, a computer controlled, parallel plate plasma reactor with cathode diameter of 24

cm. Process gases were selected as nitrogen balanced silane (2%SiH₄+ 98%N₂) with a flow rate of 145 sccm. and ammonia (NH₃) with flow rate of 50 sccm.

N₂ in the former process gas was used as carrier and dilution gas to obtain safe working conditions. The temperature was kept at 250° C with RF power of 10 W . Chemical reaction for silane and nitrous oxide mixture under RF excitation is as follows.



We deposited 0.2 μm of silicon nitride on the whole sample and later etched from places where it is unwanted. HF was the major etchant in etching the silicon nitride film with a ratio of 1:200 = HF:H₂O. The rate was around 65Å/second. Adding more water made the solvent slower and gave more control over sensitive etching.

3.1.8 Airbridge

Airbridge is extensively used in the GaAs analog devices for interconnections. The existence of air between the bridge and the wafer beneath causes low parasitic capacitance and higher ability to carry substantial current.²² The airbridges are less capacitive than the dielectric crossover by a factor of five to twenty. In our devices it was used to connect the top plate of the capacitor to ohmic metal, and to connect the Schottky metal and circuit resistors to the transmission lines.

Although airbridges are usually formed by plating, we used evaporation in our process. It is a two mark process including airpost and airbridge steps. First, a photoresist layer is exposed and developed to define the posts. The layer is hard baked at 140°C for 30 minutes in an oven and then reduced to 0.8 μm thickness by using RIE O₂ etching. Following this, a thick metal lift-off process is done in which around 1.2 μm Au is evaporated. This step connects the two airposts to each other making a bridge that sits on the top of hard baked airposts. When the resist is dissolved in acetone, the interconnect metal hangs on the air defining an airbridge from one post to the other.

Although the basic concept is straightforward, there are several number of process variations and complexities. Airbridges were never done in our laboratory, and we had to develop the process for the fabrication of high speed photodetectors. Existing metal evaporation facilities and lack of similar process history made it one of the very difficult and uncertain processes. Posts were found to get molten in the following airbridge lithography step, if the resist was not sufficiently baked and caused a serious adhesion problem while evaporating metal. On the other hand, overbake makes it difficult to remove the resist from beneath the bridge. In the airbridge formation AZ5214E was used for the bridge step spinning at 2500 rpm which gave a thickness of around 2 μm . Although 1.50 μm of Au could be lifted off with considerable effort, normally 1.0 μm was deposited in the bridge formation. Being the last step, it was always the most risky step upon which the fate of the whole sample depended. Ensuring ultra-high vacuum before metalization, doing overdevelopment to ensure the sticking of evaporated metal, sufficiently hardening the post resist are some criterion of a successful airbridge process.

3.2 Mask Design

Masks, for the fabrication of the photodetectors in our laboratory, were designed by the software WAVE MAKER. Before designing the masks, we went through an intensive process development phase and consequently gained a thorough idea about the critical mask parameters. In order to test the high speed of the photodiodes the active area was designed very small, to keep the device capacitance below 0.1 pF. For this purpose, we designed diodes of different sizes starting from $7 \times 7 \mu\text{m}^2$ to $20 \times 30 \mu\text{m}^2$. On the contrary, for the photoresponse measurements, larger active region diodes were fabricated with areas as large as $250 \times 250 \mu\text{m}^2$. Figure 3.1 shows two such diodes.

The gap width between the Schottky and ohmic contacts were varied from $2 \mu\text{m}$ (for smaller diodes) to $5 \mu\text{m}$ (for the larger diodes). In the fabricated devices, it was found that $3 \mu\text{m}$ gap width was ideal one for the best performance of the

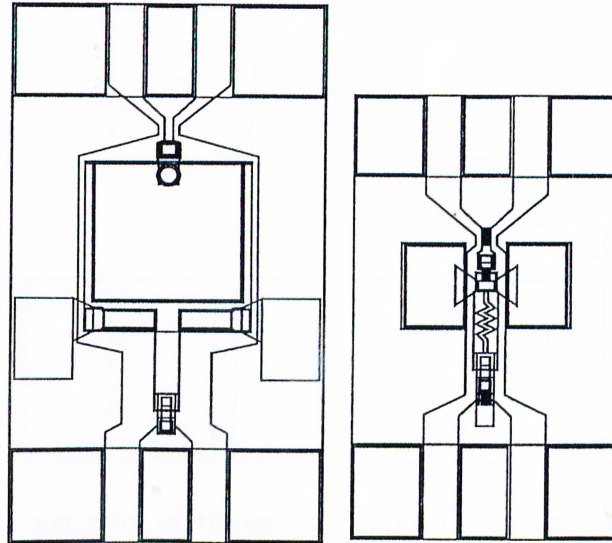


Figure 3.1: Two diode masks with different shape of active regions. The one on the left with bigger active area is used for photocurrent measurements and the one on the right with small active area is used for high speed measurements.

diodes. Because of probable misalignment of $\pm 1\mu\text{m}$ during the process, there is always a risk of short circuit between Schottky and ohmic contacts when the gap width is less than $2\mu\text{m}$ and it actually happened several times in our process.

Test patterns are also important components of the designed masks. The detector circuits had 50Ω and 100Ω resistors and two 4.5 pF capacitors. By including test patterns for these resistors and capacitors, which can be individually tested, we can measure the exact resistances and capacitances. Unlike the capacitors, the resistance varied 10% to 15% in magnitude because of fluctuating undercut during wet etching. The transmission line test patterns on the masks are used for testing the quality of the ohmic contact and the sheet resistance. Figure 3.2 shows a test pattern of a resistor and a transmission line pattern.

For RF probing, both short and long 50Ω coplanar waveguides are designed. The end pads are made thick enough by adding an extra layer of gold while forming the airbridges to connect the CPW guides with the active region of the diodes. Some bigger diodes are designed without airbridges so that even if the

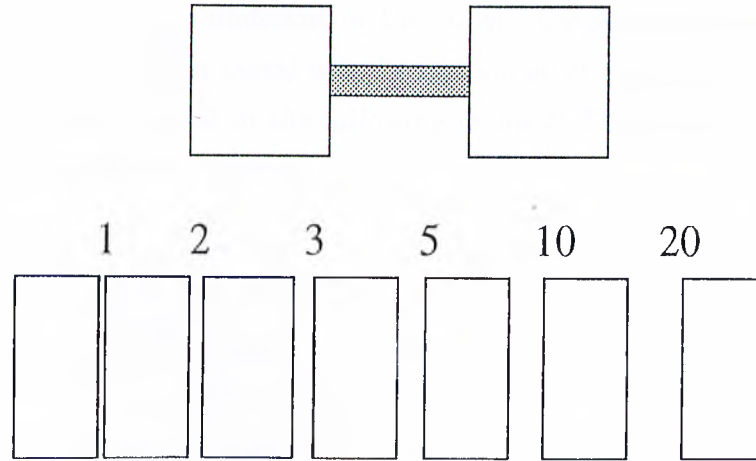


Figure 3.2: Test patterns of resistor and transmission line on the mask. The rectangular bar in between two square pads is the resistor. The numbers are the distances in microns between the transmission line test patterns.

process ends up with an unresolvable problem in the airbridge step, the labor for the sample preparation does not go in vain.

3.3 Device Processing of Photodiodes

3.3.1 Ohmic Contact Formation

In the actual wafer structure, the n^+ region was embedded at a depth of $0.4 \mu\text{m}$ in both the top and bottom illuminated samples, which is a layer of $0.5 \mu\text{m}$ in both the cases. We first patterned the resist to define the ohmic etch area and then hard baked and subsequently did RIE in order to clean the sample surfaces. Then, we etched the samples using a sulfuric acid based etchant ($1:8:80 = \text{H}_2\text{SO}_4 : \text{H}_2\text{O}_2 : \text{H}_2\text{O}$) until the n^+ region is reached. We usually overetched by $0.1 \mu\text{m}$ to guarantee that the bottom n^+ is reached all through the sample. Further over etch is avoided, as this would cause a higher spreading resistance, and an undesirably large total series resistance. Because of the presence of a InGaAs layer above the n^+ region, the etching rate was slow at the beginning. The approximate GaAs etching rate was $75 \text{\AA}/\text{sec}$ while InGaAs etching rate was $50 \text{\AA}/\text{sec}$. The etch was

isotropic, resulting in an undercut of the resist. Consequently when metal was evaporated, the laid down metal was discontinuous at the photoresist boundary. We deposited ohmic metal in the following ratios.²² The metal is then lifted off by soaking the wafer into acetone.

<i>Metal</i>	<i>ThicknessA°</i>
<i>Germanium</i>	108
<i>Gold</i>	102
<i>Germanium</i>	63
<i>Gold</i>	236
<i>Nickel</i>	100
<i>Gold</i>	2000

3.3.2 RTP (Rapid Thermal Processing)

Following the usual cleaning procedure, we prepared the samples for rapid thermal annealing. The equipment we used was not operating under automatic mode, so we had to use the manual mode. Although the recipe suggested that we keep the samples at 450°C for 20 sec, we manipulated the exact time depending on the temperature overshoot and rapidity of the annealing process.

After annealing, the quality of the ohmic contact was tested using the transmission line test structures. Further processes were continued if the specific contact resistance was in the range of 10^{-6} ohm-cm². We thoroughly maintained this test to scan out the unworkable samples so that they were not allowed through the tedious seven step photodiode processes. Unfortunately, due to an unalterable mistake during MBE growth, the top illumination sample had low or almost no doping concentration at n^+ region. This resulted in a very bad ohmic contact, i.e., three orders worse than the expected one. So we just fabricated some photodiodes with that sample to test the photoresponsivity.

The quality of the ohmic metalization can also be tested by inspecting it using an optical microscope. The actual ohmic metal will appear splotchy, having dark and light spots, almost like a piece of Swiss cheese, having lots of patterns

displaying the presence of Ni alloys. Good quality ohmic contacts were obtained even at both 430° C and 500° C although the best was at around 450°C to 460°C.

3.3.3 Mesa Isolation

After a successful ohmic metalization, we isolated the mesas and etched away all the unwanted doped regions to reach the semi-insulating GaAs layer immediately above the Bragg mirror. In this step, while defining the photoresist mask, we allowed reasonable overdevelopment to ensure uniform cleanliness all over the samples. After hard bake at 120°C for about 50 sec, we cleaned the samples in the RIE O₂ plasma for about 2 minutes. Making repeated use of DekTak stylus profilometer, we etched the samples to reach the insulating GaAs layer which is 1000Å in thickness. Below this insulating layer, we have bottom mirror containing layer of GaAs and AlAs. Lack of precaution might expose the AlAs layer which is highly active in the open air and oxidizes in a very short time to result in a amorphous non-sticky oxide. Again the presence of different material in the samples, caused large fluctuations in the etching rates. So frequent monitoring of the etching depth was necessary in this process.

We etched away 0.90 μm to remove all the doped layers from the wafer. In the mesa isolation process, the circuit resistors, active diode regions including the ohmic and Schottky metal areas and the regions of test patterns were isolated. We found the etchant becoming weak with time because of the fickle life time of H₂O₂. Even the rate changes within 5 minute were considerably great and so without monitoring there could be great deviations in the expected depth of etching. In order to get rid of measuring the changing etching rates of various layers we developed an strategy. We first etched the samples for a considerable time to ensure around 5000 to 6000Å of etching and thus reached the n⁺ region of the wafer. Etching the samples in the mentioned solution for 1 minute served this purpose. Then we found out the etching rates of the n⁺ region and thereby completed the mesa isolation. The undercut in mesa isolation was found to be around 1μm for 1μm depth. We included this in our mask design to preserve the

expected resistance of the circuit resistors. Another probable problem was the variation of etch rate at different regions of the sample. It was mostly prevented by developing the sample very well and cleaning it with RIE. Even after taking all sorts of precautions, this variation was observed which might partially pertain to the sensitivity of the DekTak .

3.3.4 Interconnect metal

In order to connect the diode active regions to either transmission lines or microwave compatible pads, an interconnect metal layer was deposited over the insulating GaAs. It also served the purpose of the lower plate of the circuit capacitors. Gold was the major component of the interconnect metal although Ti was first used for adhesion. Spinning the samples at 2500 rpm gave around $1.9 \mu\text{m}$ of photoresist thickness. Hardening the resist in chlorobenzene immediately after the exposure is a prerequisite for a successful lift-off process. We deposited 200\AA of Ti and 2500\AA of Au in the interconnect metalization step. Immediately before the deposition of the metal, we cleaned the samples with dilute HF to enhance adhesion. When lift-off seemed to be slow, we applied a short ultrasonic perturbation to quicken the process.

3.3.5 Schottky Metalization

Schottky metal was deposited over the n^- region at a horizontal distance of $2\mu\text{m}$ from the ohmic metal. In the top illuminated sample, Schottky metal thickness varied from 100\AA to 300\AA . It had to be thin enough to allow transmission of light. Normally a thin Au layer of 100\AA does not stick very well to sample. Schottky metal lies above all other layers causing a risk of being scratched out, when the sample is handled without much care. So, we performed Schottky metalization immediately before nitride deposition so that all sorts of external harms could be prevented. We found that over exposure and overdevelopment enhanced sticking property. Although Ti could be added to serve this purpose, it was found to cause degradation in the Schottky quality.

3.3.6 Dielectric Deposition

A thin Si_3N_4 film of 2000\AA thickness was deposited all over sample to achieve three purposes. First, it is used as dielectric slab in between the capacitor plates. Second, it covers the whole sample with an antireflection coating. Third, it protects the samples from the atmosphere. The process is discussed earlier in the subsection related to PECVD. Si_3N_4 film which is deposited at 250°C is a glass like sticky substance that covers the whole sample isotropically. Later, Si_3N_4 is

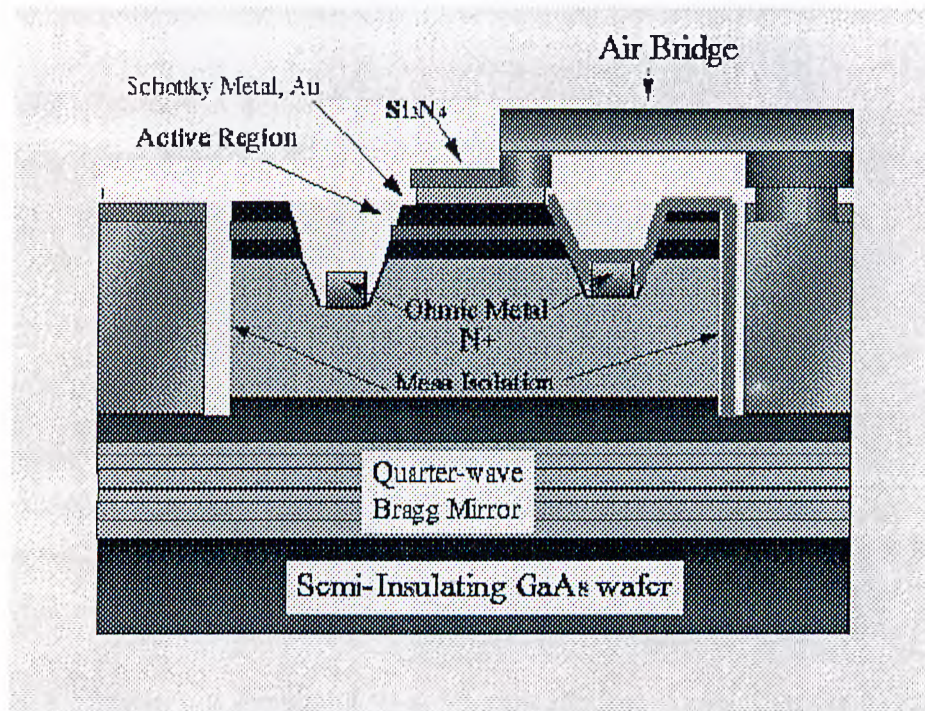


Figure 3.3: Crosssection of a photodiode showing different components.

etched by HF solution to create some openings in order to connect the diode to the interconnect metal and bridge the circuit capacitors with the active regions. Si_3N_4 is also etched away from the end pads of the interconnect metals so that diodes can be biased from outside using microwave probes. Precaution was taken to prevent the RF reflection during PECVD process because the thickness of the film might change if any partial reflection was allowed. Besides using Dektak for measuring the thickness of the film, we used the color chart to estimate the

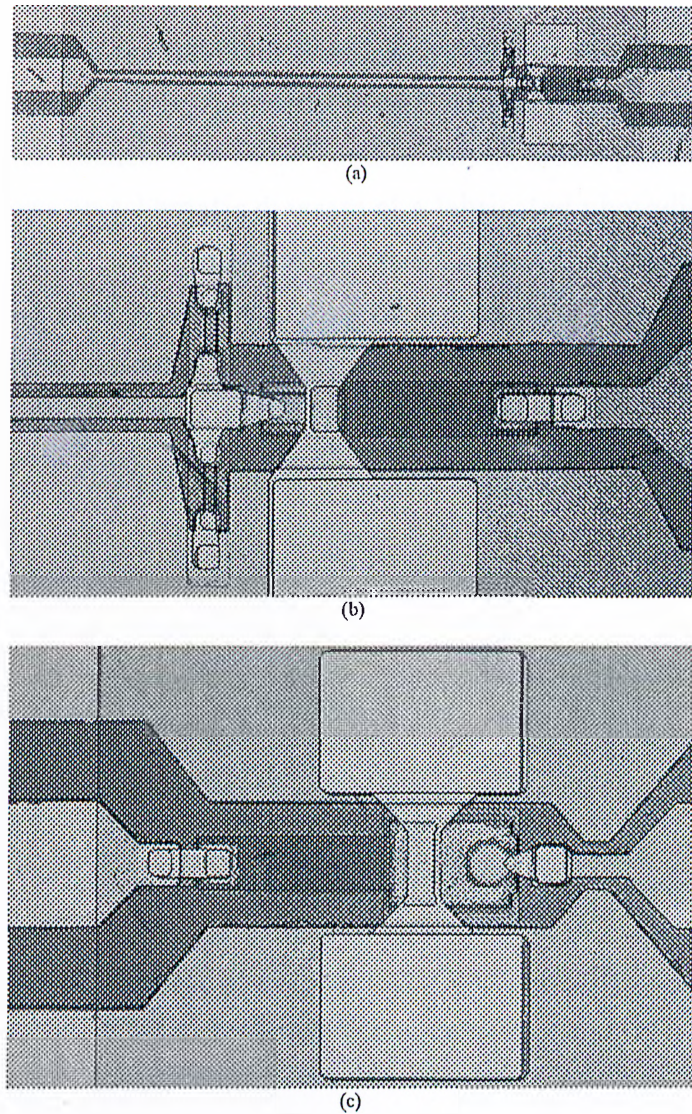


Figure 3.4: Photomicrographs of two different diodes. The active region of diode (a) is zoomed in figure (b). Figure (c) is a large area diode.

thickness of the film which is dark red for 2000\AA .

3.3.7 Airbridge

High speed photodetector process was completed by the fabrication of airbridge. This is a two mask level process, including airpost and airconnect steps. First, we exposed and developed a thin photoresist layer to define the airposts of the airbridges. Then the samples were hard baked at 140°C so that the airpost resist

doesn't get dissolved in the following lithography step of airbridge formation. We then, deposited $1\mu\text{m}$ of airbridge metal in the sample prepared carefully by the application of Chlorobenzene to cause good undercut in the photoresist patterns.

Figure 3.3 shows an schematic diagram of a fabricated photodiode. Figure 3.4 shows photographs of two diodes with different sizes. The longer diode (a) was designed for future electro-optic sampling measurements. Figure 3.4 (c) shows a typical diode with a diameter of 30 microns. The wing like structures on both sides are circuit capacitors and the darker islands are resistors.

Chapter 4

Resonant Cavity Enhancement

In chapter 1, we stated that in the design of a high-speed Schottky barrier photodiode, the thickness of the active layer is usually kept thin in order to achieve small transit times for high speed operation. However, using a thin active layer also reduces the effective absorption depth for the wavelength of interest. A detector with an absorbing layer thicker than $1.6 \mu m$ achieves quantum efficiencies greater than 80%, but yields a very poor speed performance as a consequence of longer transit time in the thicker depletion region.

In order to increase the optical absorption in the active region of the detector without decreasing the bandwidth of the device, Chin and Chang²³ first proposed resonance-enhanced absorption by adding a multilayer reflector to the thin active layer of the diode. In such structures, the device functions largely as before, but is subject to the effects of the cavity, mainly wavelength selectivity and a large enhancement of the resonant optical field. The increased optical field allows photodetectors to be made thinner and therefore faster, while simultaneously increasing the quantum efficiency at the resonant wavelength.²⁴ This technique has been applied to a number of photodetectors such as avalanche²⁵ and p-i-n photodiodes²⁶ and found to be very effective. However, the absorption thickness cannot be reduced indefinitely. As an example, a photodiode with $25 \mu m$ diameter and $0.1\text{-}\mu m$ absorption thickness, has a junction capacitance of 0.75 pF corresponding to an RC time constant of 25 ps . Therefore, the response speed

for such a detector will be limited by the RC time constant and the advantage of reducing the absorption layer thickness to lower the carrier transit time will no longer be important in this case. Furthermore, the quantum efficiency will be around 10% which is not practical for most applications. Another technique of enhancing the quantum efficiency is to use an antireflection coating which is optimized to feed the reflected power back to the main cavity in which the absorbing region is placed. In this chapter, we discuss how the quantum efficiencies of the design structures shown in Figure 4.1 were enhanced.

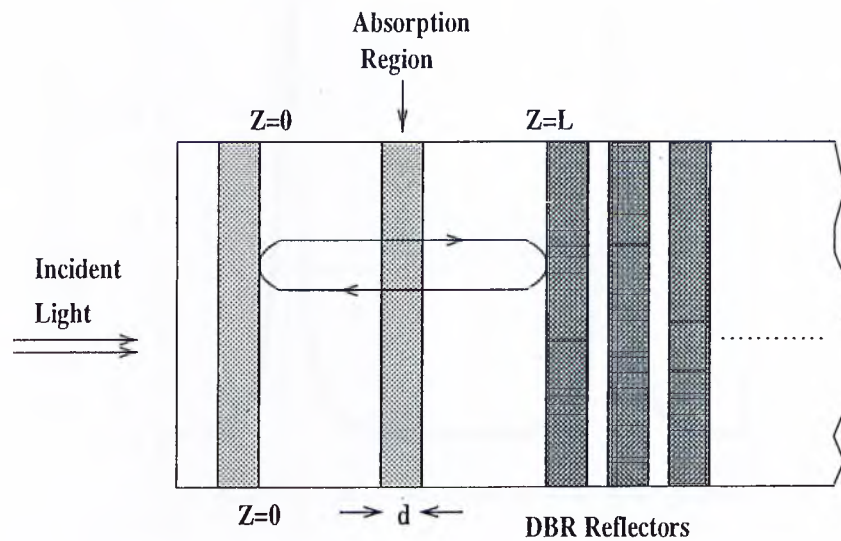


Figure 4.1: Analysis model of an RCE photodetector. The active region of thickness d is a small bandgap semiconductor. The top and bottom distributed Bragg reflection mirrors consist of alternating layers of non-absorbing larger bandgap materials.

4.1 Mechanism of Efficiency Enhancement with a Resonant Cavity

With the aim of increasing the quantum efficiency without decreasing the bandwidth of the device, we placed a thin absorbing layer in a Fabry-Perot microcavity as is shown in Figure 4.1. In this way, the optical field cycles

in the cavity, being partially absorbed each time crossing the thin absorbing layer, hence a multiple-pass detection is obtained. The consequence of the multiple-pass detection scheme is increased quantum efficiency at the resonant wavelengths. The quantum efficiency of RCE photodetectors with lossless mirrors was calculated to be,²³

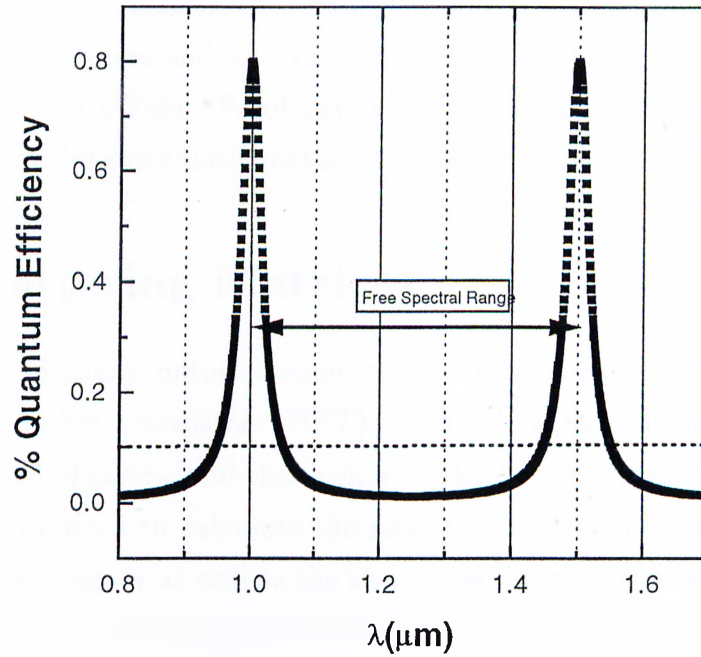


Figure 4.2: Quantum efficiency of an RCE photodiode. The dashed straight line shows the maximum attainable quantum efficiency for a conventional photodetector of same thickness.

$$\eta = \left\{ \frac{(1 + R_2 e^{-\alpha d})}{1 - \sqrt{R_1 R_2} e^{-\alpha d} \cos(2kL + \psi_1 + \psi_2) + R_1 R_2 e^{-2\alpha d}} \right\} (1 - R_1)(1 - e^{-\alpha d}) \quad (4.1)$$

where R_1 and R_2 are the top and bottom mirror reflectivities respectively, k is the propagation constant, L is the cavity length and ψ_1 and ψ_2 are the phase shifts introduced by the top and bottom mirrors respectively. Equation 4.1 gives $\eta = 0.66$ for $d = 0.1 \mu m$ at the resonant wavelengths. The maximum attainable

quantum efficiency for the same detector without the resonant cavity would be 0.09. The Equation 4.1 is plotted in Figure 4.2, for $R_1 = 0.8$, $R_2 = 0.95$, $\alpha d = 0.1$, and the quantum efficiency of a conventional photodetector with same αd is shown by the dashed line. In Figure 4.2, the characteristics of the photoresponse of an RCE photodetector is easily identified: increased quantum efficiency at the resonant wavelengths is the consequence of the constructive interference between the forward and backward propagating fields, whereas the quantum efficiency at the off-resonant wavelengths decreases due to destructive interference.

In order to understand the mechanism of enhancing the efficiency of the detectors by using a Fabry-Perot cavity, we briefly discuss the S-matrix method which is a powerful systematic method to analyze multilayer optical structures.³¹

4.2 Scattering Matrices

The analysis of many optoelectronic components such as *p-i-n*, Schottky and heterojunction phototransistors (HPT) may be done by considering these devices to be composed of layers, and then using the tools to analyze multilayer films. In the analysis, we need to calculate the reflection and transmission of the optical power at any boundary as well as the absorption in various lossy layers. Different methods like transmission and transfer matrices, impedance transformation, self consistent consideration of the optical field and S-matrix (scattering-matrix) are employed to analyze multilayer stacks and to evaluate the exact field distribution in passive structures.²⁷

In the S-matrix approach, each material layer in the stack is considered as a two port transmission line with a normalized characteristic impedance $Z = 1/n$ where n is the refractive index of the medium. Travelling waves are used to characterize the optical two ports and the waves leaving the two ports are given in terms of waves entering the two ports.

In a specific optical median generally for a fixed energy E , we have a forward wave ϕ_f and a reverse wave ϕ_r at any point, i.e.,

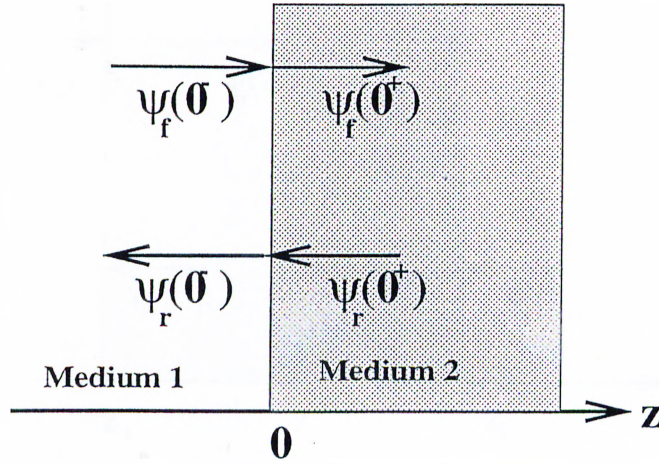


Figure 4.3: Changes of wave functions at the interface two media. For simplicity, a one-dimensional problem is assumed.

$$\phi(z) = \phi_f(z) + \phi_r(z) \quad (4.2)$$

Now considering the optical interface at $z = 0$ as shown in Figure 4.3, $\phi_f(0^+)$ denotes the incident wave for $z > 0$, $\phi_r(0^-)$ is the reflected wave for $z < 0$, $\phi_f(0^-)$ is the incident wave for $z < 0$, and $\phi_r(0^+)$ is the reflected wave for $z > 0$. Since the wave equation is linear, superposition of the wave equations governing both the right and left bound electromagnetic (EM) wave yields

$$\begin{bmatrix} \phi_f(0^+) \\ \phi_r(0^-) \end{bmatrix} = \begin{bmatrix} t & r' \\ r & t' \end{bmatrix} \begin{bmatrix} \phi_f(0^-) \\ \phi_r(0^+) \end{bmatrix} \quad (4.3)$$

where, t is the transmission coefficient of EM wave travelling from left to right, r is the reflection coefficient of EM wave traveling from left to right, t' is the transmission coefficient of EM wave travelling from right to left and r' is the reflection coefficient of EM wave traveling from right to left. The (2×2) matrix on the right side of the Equation 4.3 is known as the scattering matrix or S-matrix.

Next we apply the argument to develop the rules for cascading the matrices. As shown in Figure 4.4, we have two sections divided by three points z_1 , z_2 , and z_3 . These are the geometric points. There are no real interfaces at these points, and hence no change of wave function at each point is expected. However, if we

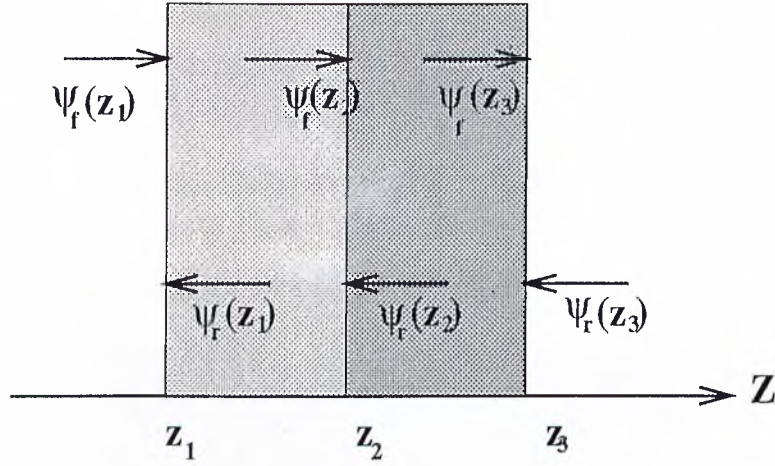


Figure 4.4: Schematic diagram of the wave function traveling through two sections of medium, .

take the whole section as one piece, there are two components of waves coming into the section and two components of waves going out of the section. The relationship of these function can be expressed in a way similar to Equation 4.3, but with different S-matrices. Therefore, for $z_1 - z_2$ section, we have

$$\begin{bmatrix} \Psi_f(z_2) \\ \Psi_r(z_1) \end{bmatrix} = \begin{bmatrix} t_{21} & r'_{21} \\ r_{21} & t'_{21} \end{bmatrix} \begin{bmatrix} \Psi_f(z_1) \\ \Psi_r(z_2) \end{bmatrix} \quad (4.4)$$

where t_{21} and r_{21} are the respectively transmission and reflection coefficients for the electromagnetic wave traveling from port 1 to port 2. For $z_2 - z_3$ section, the expression is given by

$$\begin{bmatrix} \Psi_f(z_3) \\ \Psi_r(z_2) \end{bmatrix} = \begin{bmatrix} t_{32} & r'_{32} \\ r_{32} & t'_{32} \end{bmatrix} \begin{bmatrix} \Psi_f(z_2) \\ \Psi_r(z_3) \end{bmatrix} \quad (4.5)$$

For the cascade of the these two sections, i.e., for $z_1 - z_3$ section we obtain

$$\begin{bmatrix} \Psi_f(z_3) \\ \Psi_r(z_1) \end{bmatrix} = \begin{bmatrix} t_{31} & r'_{31} \\ r_{31} & t'_{31} \end{bmatrix} \begin{bmatrix} \Psi_f(z_1) \\ \Psi_r(z_3) \end{bmatrix} \quad (4.6)$$

where,

$$\begin{aligned}
t_{31} &= \frac{t_{32}}{(1-r'_{21}r_{32})}t_{21} \\
r_{31} &= r_{21} + \frac{t'_{21}r_{32}}{1-r'_{21}r_{32}}t_{21} \\
r'_{31} &= r'_{32} + \frac{t_{32}}{1-r'_{21}r_{32}}r'_{21}t'_{32} \\
t'_{31} &= \frac{t'_{21}}{1-r_{32}r'_{21}}t'_{32}
\end{aligned} \tag{4.7}$$

are the elements of S-matrix for two ports.

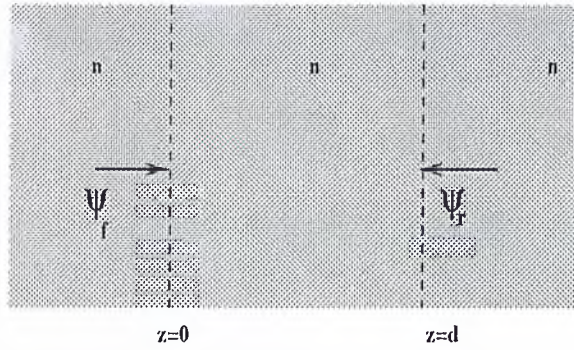


Figure 4.5: Simple optical layer without any interface

If light is assumed to be consisting of plane harmonic waves, expressed by $\Psi = \Psi_0 e^{i(kz - \omega t)}$, then the S-matrix method can be used to the simplified one dimensional problem of finding all field phasors Ψ_{fi}, Ψ_{ri} , where $i = 1, 2$. In Figure 4.5, there is no physical interface to cause reflection. So forward and backward propagating field phasors undergo a phase shift due to the length d of the medium. In the case of a complex refractive index, the magnitudes of the field phasors are also modified corresponding to a lossy medium. The forward and backward propagating fields can be written as

$$\begin{bmatrix} \Psi_f(z = d^+) \\ \Psi_r(z = 0^-) \end{bmatrix} = \begin{bmatrix} e^{ikd - \frac{\alpha}{2}d} & 0 \\ 0 & e^{ikd - \frac{\alpha}{2}d} \end{bmatrix} \begin{bmatrix} \Psi_f(z = 0^-) \\ \Psi_r(z = d^+) \end{bmatrix} \tag{4.8}$$

where $k = 2\pi n_R/\lambda$ and $\alpha = 4\pi n_I/\lambda$ are called the propagation and the attenuation constants respectively and λ is the free-space wavelength of the incident light. The (2×2) matrix on the right side of Equation 4.8 is the S-matrix for the layer in Figure 4.5.

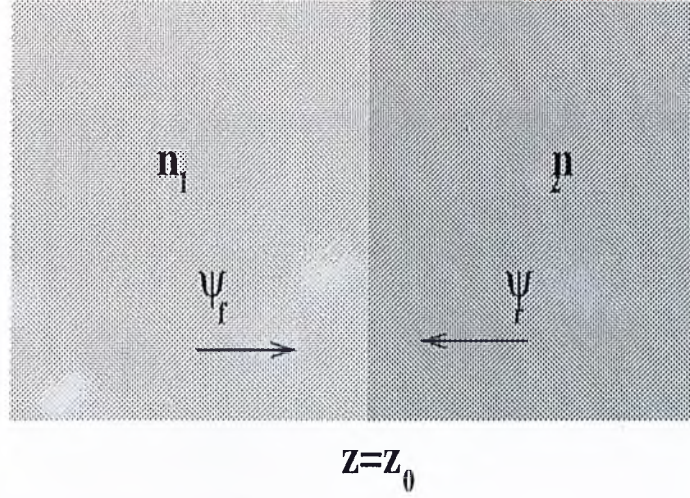


Figure 4.6: Optical layer with an interface.

In the case of a physical interface at $z = z_0$ between two semi-infinite media with refractive indices n_1 and n_2 (as shown in Figure 4.6), the reflected and transmitted fields may be written in S-matrix notation as

$$\begin{bmatrix} \Psi_f(z = z_0^+) \\ \Psi_r(z = z_0^-) \end{bmatrix} = \begin{bmatrix} t_{21} & r'_{21} \\ r_{21} & t'_{21} \end{bmatrix} \begin{bmatrix} \Psi_f(z = z_0^-) \\ \Psi_r(z_0^+) \end{bmatrix} \quad (4.9)$$

where

$$\begin{aligned} t_{21} &= \frac{2n_1}{n_1 + n_2} \\ t_{12} &= \frac{2n_2}{n_1 + n_2} \\ r_{21} &= \frac{n_1 - n_2}{n_1 + n_2} \\ r_{12} &= \frac{n_2 - n_1}{n_1 + n_2} \end{aligned} \quad (4.10)$$

are Fresnel's reflection and transmission coefficients for normal incidents. Using the two S-matrices in Equations 4.8 and 4.9, and the rules for cascading S-matrices, S-matrix representation of any optical multilayer stack may be calculated.²⁸

Using the S-matrix formalism for a structure shown in Figure 4.7, for simplicity, it can be shown that the power absorbed in the active region of the diode is given as,³¹

$$P_A = P_{in} \left(\frac{n_2}{n_1} |t_{12}|^2 \frac{1 - |r_{24}|^2}{|1 - r_{24}r_{21}|^2} - \frac{n_3}{n_1} |t_{13}|^2 \frac{1 - |r_{34}|^2}{|1 - r_{24}r_{21}|^2} \right) \quad (4.11)$$

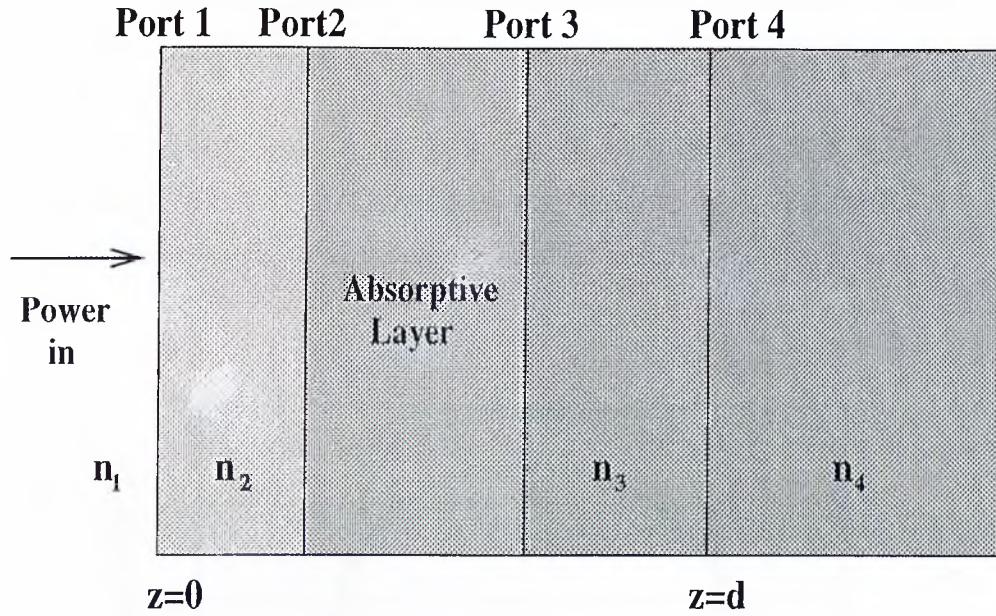


Figure 4.7: Absorption layer in a stack.

Since there are both forward and backward traveling waves in a multilayer stack, there is a standing wave pattern due to the destructive and constructive interference of the opposite propagating waves. In some cases, it is desirable to calculate this field distribution. The knowledge of the field distribution within the cavity helps us to place the absorption region in the exact location. The E-field at an arbitrary position z in the stack can be written as,³¹

$$\Psi(z) = (1 + r_{zd}) \frac{t_{0z}}{1 - r_{zd}r_{z0}} \Psi_f(0) \quad (4.12)$$

where $z=0$ and $z=d$ are the two ends of the stack.

4.3 The Components of the Resonant Cavity

The Schottky diode photodetector can be easily integrated with a Bragg reflector to form an RCE photodetector. The basic components of the resulting resonant

cavity consist of a Au layer, serving both as a Schottky metal and a semi-transparent top mirror, and a high-reflectivity multilayer bottom mirror. The bottom mirror of the cavity is formed with alternating $\lambda/4$ - $\lambda/4$ AlAs/GaAs layers. Both AlAs and GaAs should be transparent at the design wavelength. On top of the bottom mirror, an undoped GaAs buffer, an N^+ GaAs layer for ohmic contacts, and an N^- GaAs depletion layer follow. Inside the N^- GaAs layer, a thin InGaAs absorbing layer is used as the photoactive region.

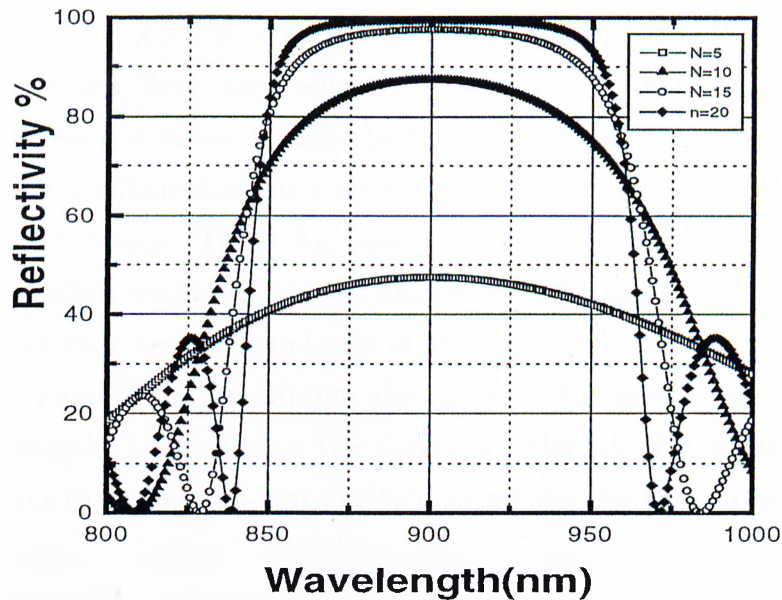


Figure 4.8: Reflectivity of QWS for different numbers of stack pairs.

4.3.1 The Bottom Reflector

A typical GaAs based quarter wave stack (QWS) consists of alternating $\lambda/4$ - $\lambda/4$ high index (n_H) GaAs and low index (n_L) AlAs layers on semi-insulating GaAs substrate. This QWS can be used as bottom mirror of our cavity. Using the S-matrix method described earlier, the QWS structure is analyzed and the power

reflectance at the central wavelength is given by,

$$R_{max} = \left[\frac{n_H^{2N} - n_L^{2N}}{n_H^{2N} + n_L^{2N}} \right]^2 \quad (4.13)$$

where N is the number of low-index layers in the stack. Figure 4.8 shows the reflectance of $N=5, 10, 15$ and 15 layers AlAs/GaAs ($n_L = 3, n_H = 3.5$) QWS.

4.3.2 The Top Mirror

In RCE Schottky photodiodes, the top Au layer is used both as the Schottky contact and as the top mirror of the resonant cavity. For bottom illumination, the top mirror is a thick high reflectivity layer ($t_m > 1000 \text{ \AA}$, $R = 0.94$). The quantum efficiency is insensitive to the thickness of the Au layer in this regime. The absorption coefficient of Au is very high compared to that of other materials of the resonant cavity. Thick Au layer can absorb a considerable part of the incident light when we illuminate the diodes from the top surface. Consequently we had to optimize the the thickness of the top mirror which was found to be 80 \AA . It was found³¹ that maximum absorption in the metal occurs at a slightly longer wavelength (1-2 nm) than the design wavelength of $\lambda = 900 \text{ nm}$. This is due to the fact that, the resonant cavity maximizing the absorption in the metal is slightly longer (including the thickness of the metallic layer), than the resonant cavity maximizing the quantum efficiency.

4.4 Device Structure

Using the simulation results described earlier, we designed two structures for MBE growth. The first structure which will be called RCE1, is designed for top illumination. The second structure is designed for bottom illumination and will be called RCE2. Both structures were designed for an operation wavelength of 900 nm. A schematic diagram describing the epilayer is shown in Figure 4.9.

In the RCE1 sample, we have fifteen pairs of quarter-wave GaAs(638 \AA)/AlAs(755 \AA) reflector layer on top of semi-insulating GaAs. Both AlAs and

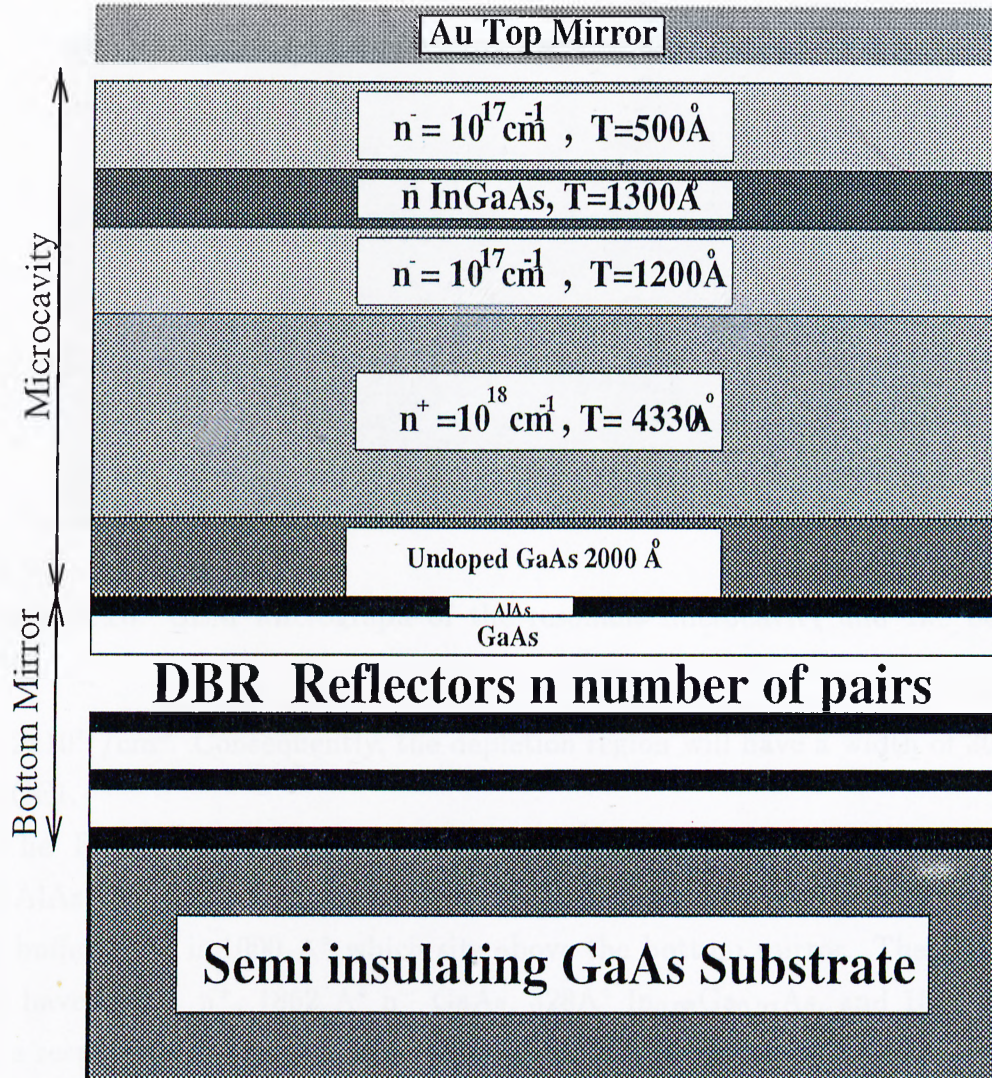


Figure 4.9: Epitaxial layer design of a top illuminated resonant cavity enhanced photodiode wafer. In bottom illuminated wafer, the InGaAs layer is 343 Angstrom. Number of pairs of GaAs/AlAs bottom mirror is 15 in the top and 10 in the bottom illuminated sample. The top mirror is Au layer which we deposit over the surface of the wafer during the fabrication.

GaAs are transparent at the design wavelength of 900 nm. The reflector layers are followed by a 2000 \AA GaAs buffer layer, 4330 \AA n^+ region ($N^+ = 3 \times 10^{18} / \text{cm}^3$) for ohmic contact, an active layer of 1200 \AA n^- GaAs, 1300 \AA of $\text{In}_{0.08}\text{Ga}_{0.92}\text{As}$ and finally 500 \AA of n^- GaAs. All three N^- layers have a doping concentration

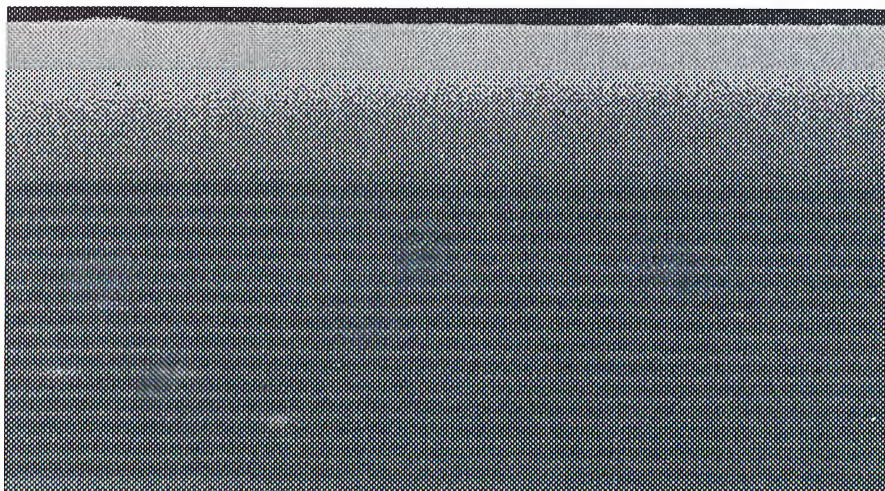


Figure 4.10: SEM micrograph of the resonant microcavity and the bottom mirror

of $1.2 \times 10^{17} / \text{cm}^3$. Consequently, the depletion region will have a width of 3000 \AA in RCE1.

The RCE2 sample has 10 pairs of reflector of quarter-wave GaAs(638 \AA)/AlAs(755 \AA) layers and similar doped regions with different thicknesses. The buffer layer is 1000 \AA which sits above the bottom mirror. The structure then have 5000 \AA n^+ , 1862 \AA n^- GaAs, 328 \AA $\text{In}_{0.08}\text{Ga}_{0.92}\text{As}$, and 1556 \AA n^- GaAs respectively. The depletion region in RCE2 is, therefore, 3746 \AA in width when fully biased.

The presence of the $\text{In}_{0.08}\text{Ga}_{0.92}\text{As}$ layer in between the n^- GaAs layers in the depletion region in both the cases allows the detection of longer wavelength than the corresponding wavelength of GaAs which is 870 nm . The relation between the In concentration x and the bandgap edge $E_o(x)$ of $\text{In}_x\text{Ga}_{1-x}\text{As}$ is given by³⁰

$$E_o(x) = 1.42 - 1.53x + 0.45x^2 \quad (4.14)$$

Using the $x = 0.08$ for the present case, the bandgap wavelength of InGaAs is found to be $\lambda_g = 953 \text{ nm}$ which is well above our design wavelength of 900 nm .

4.5 Reflection Properties of MBE Structures

After designing the cavity structures, the wafers were grown at the MBE facility of Iowa State University. Before doing any process with the wafers, we used a spectrophotometer to investigate the reflection profile. RCE1 was perfectly grown and showed a peak at 915 nm while RCE2 had a shifted resonance at 940 nm which might be the result of deviations in the thickness of the the cavity layers. When diodes are fabricated this resonance shifts around 20 nm to lower wavelengths resulting in a peak quantum efficiency around 900 nm wavelength in RCE1 sample and 920 nm in RCE2. Figures 4.11 and 4.12 shows the spectrophotometric analysis of the two samples. In order to investigate the quality of the wafer structures, we checked one of the samples using SEM and clearly viewed the embedded mirror layers and other regions of the cavity. (Figure 4.10)

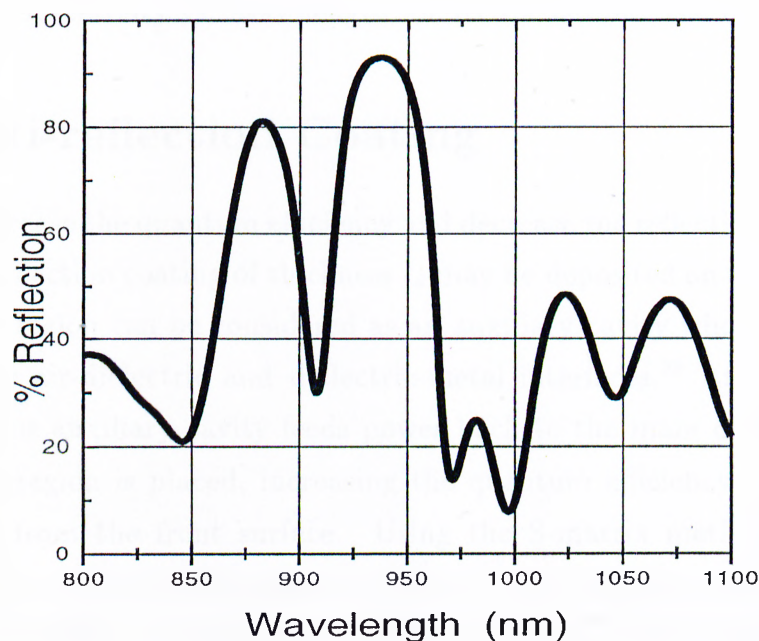


Figure 4.11: Reflectivity with respect to the wavelength for RCE1 sample, the resonance is at 915nm.

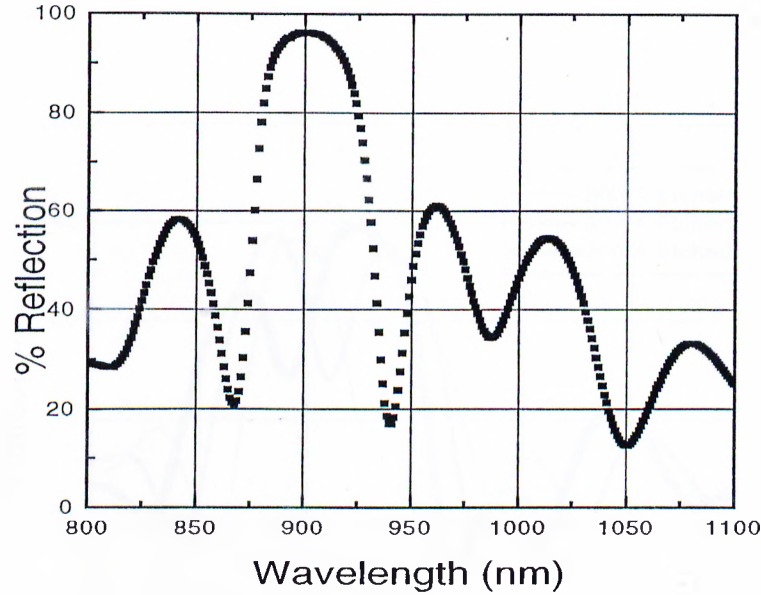


Figure 4.12: Reflectivity vs. wavelength for RCE2 sample, the resonance is at 940nm.

4.6 Anti-reflection Coating

In order to increase the quantum efficiency and decrease the reflection, a dielectric (Si_3N_4) anti-reflection coating of thickness t_d may be deposited on the Au mirror. The dielectric region can be considered as an auxiliary cavity whose mirrors are formed by the air-dielectric and dielectric-metal interfaces.²⁹ At the resonant wavelength, this auxiliary cavity feeds power back to the main cavity in which the absorbing region is placed, increasing the quantum efficiency and reducing the reflection from the front surface. Using the S-matrix method, we found the dependence of the peak quantum efficiency on the metal and dielectric thicknesses. The film can enhance the efficiency only in the top illuminated devices. Applying the simulation method, it was found that 2200 Å dielectric film with RCE1 and 1500 Å with the top illuminated RCE2 can optimize the efficiencies of the photodiodes.

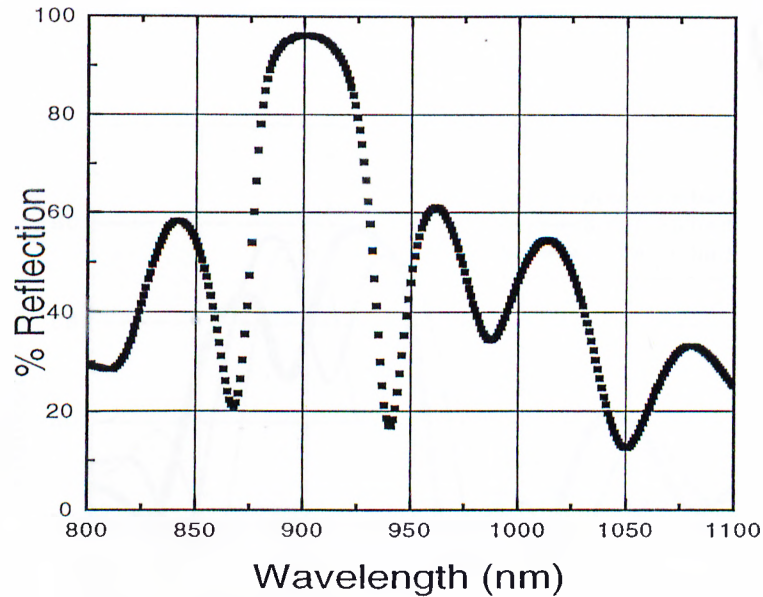


Figure 4.12: Reflectivity vs. wavelength for RCE2 sample, the resonance is at 940nm.

4.6 Anti-reflection Coating

In order to increase the quantum efficiency and decrease the reflection, a dielectric (Si_3N_4) anti-reflection coating of thickness t_d may be deposited on the Au mirror. The dielectric region can be considered as an auxiliary cavity whose mirrors are formed by the air-dielectric and dielectric-metal interfaces.²⁹ At the resonant wavelength, this auxiliary cavity feeds power back to the main cavity in which the absorbing region is placed, increasing the quantum efficiency and reducing the reflection from the front surface. Using the S-matrix method, we found the dependence of the peak quantum efficiency on the metal and dielectric thicknesses. The film can enhance the efficiency only in the top illuminated devices. Applying the simulation method, it was found that 2200 Å dielectric film with RCE1 and 1500 Å with the top illuminated RCE2 can optimize the efficiencies of the photodiodes.

4.7 Wavelength Tuning

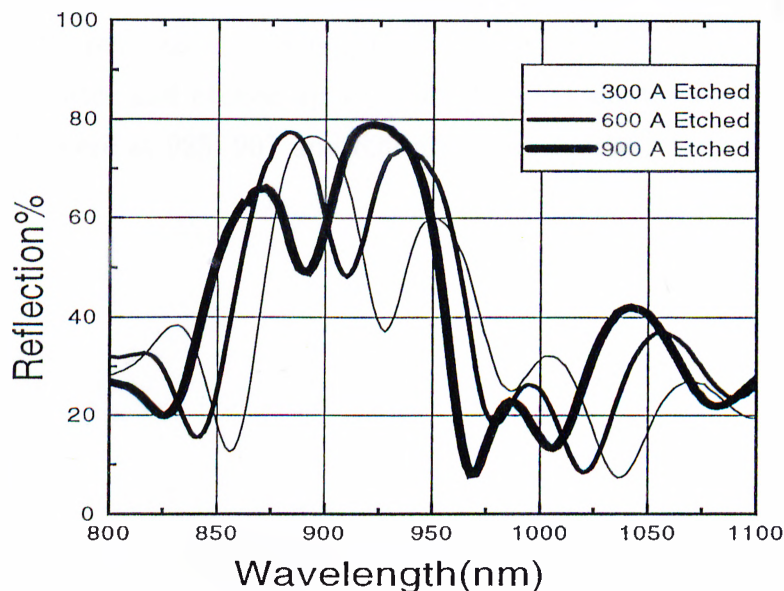


Figure 4.13: The shifts of the resonance wavelength with cavity etching.

The wavelength λ_p corresponding to the peak quantum efficiency η_p can be tuned by changing the resonance cavity length. This has to be achieved during MBE (molecular beam epitaxy) growth of the wafer. The post-growth modification of the cavity length may be done by etching of the top surface. This results in a shorter cavity length and the peak wavelength shifts to smaller values (down-tuning). To achieve a shift of the peak wavelength towards longer values (up-tuning), the thicknesses of the metallic and dielectric layers may be varied. But, up-tuning achieved with these methods will be very limited when compared to down-tuning. For the bottom illuminated device, up-tuning is not possible since the necessary metal thickness for this design is very large and has no effect on the resonant wavelength.

When we illuminated the RCE2 diodes from the top it was found to show resonance at 920 nm. Using the S-matrix simulation, we found that by etching

320 Å, the resonance wavelength could be shifted to 900 nm. We prepared photodiodes by etching 320 Å of the RCE2 sample and found the peak quantum efficiency sharp at 900nm. We later etched 600 and 900 Å of the RCE2 sample and found the resonance at 882 nm and 860 nm respectively. Figure 4.13 shows the shift of the resonance wavelength of the cavity with etching. We used the spectrophotometer and etched up to three different depths of 300, 600 and 900 Å. The peaks were at 925, 907 and 890 nm respectively.

Chapter 5

Measurement and Results

In this chapter, we present the experimental results obtained from the fabricated devices. We investigated two different RCE Schottky photodiode structures, named RCE1 and RCE2. The major difference between the structures is that RCE1 has a 1300Å absorbing region, while RCE2 has a 343Å absorbing region. Although RCE2 was optimized for bottom illumination and RCE1 for top illumination, we illuminated both of the samples from the top surface owing to the lack of experimental apparatus to illuminate the samples from the bottom. Therefore, all the data that will be presented in this chapter is obtained by illuminating the devices from the top surface. We first present the results of reflectance spectra analysis of the grown wafers. Comparison between two different RCE1 wafers obtained from different MBE growers is also given in order to have an idea about the difficulties of growing a good sample. In order to achieve the desired resonant wavelength, some portion of the RCE2 wafer was etched which caused a down-shift of the resonant wavelength. We then present current-voltage characteristics of the fabricated diodes. The high speed measurement techniques and the experimental results are given at the end of the chapter.

5.1 Photospectrometric Analysis

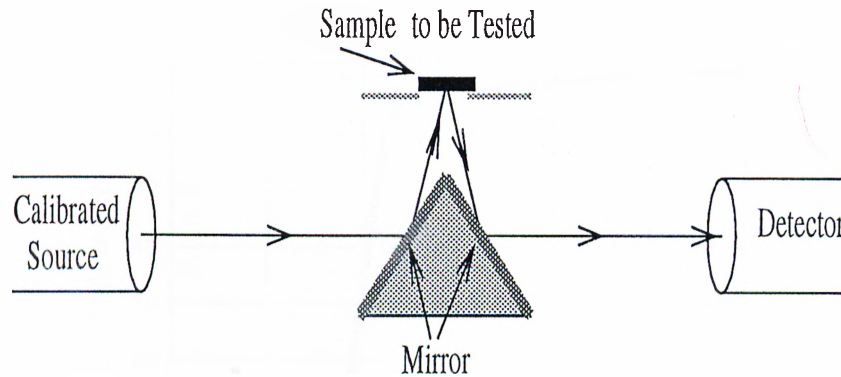


Figure 5.1: Experimental setup for measuring the reflectivity.

We performed the photospectral measurements using two different methods. First, CARY photospectrometer along with a specular reflection setup was used to measure the reflectivity of both the structures. Second, blackbody light generated by a 50W Tungsten halogen light bulb was passed through a monochromator (CVI Model CM110) to obtain monochromatic light. The output was later focused on the wafers and the fabricated devices for reflectivity and photoresponse measurements.

5.1.1 Reflectivity Measurements

In order to check the accuracy of the designed structure, front-surface reflectivity was measured by a photospectrometer before beginning any fabrication process. We used the reflectivity setup shown in the figure 5.1 to measure the reflectivity of the two samples. A silver (Ag) mirror manufactured by New Focus which has almost 100% reflectivity in the wavelengths of 800 nm to 1100 nm was used as a reference mirror. The setup in Figure 5.1 has two reflectors inclined at an angle so that horizontal light coming from the left is reflected from the first mirror and reach the wafer-under test at an incident angle of 7° . The light reflects from the wafer back to the second mirror which then directs the light to the detectors of the spectrophotometer.

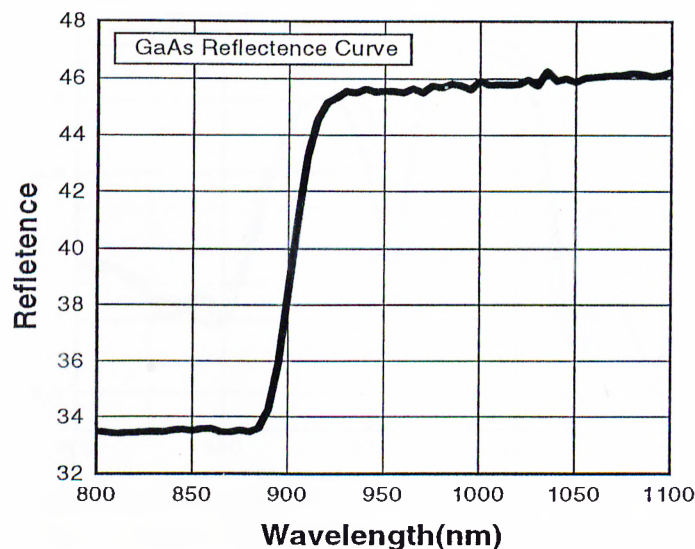


Figure 5.2: Reflectivity of a bare GaAs wafer.

We first measured the reflectivity of a bare GaAs wafer to check the reliability of the equipment. Figure 5.2 shows the reflectance curve of bare GaAs. As expected theoretically, the reflectivity showed a drop at wavelengths less than 870 nm due to absorption. The reflectivity of the RCE1 and RCE2 samples were later measured. The measured and simulated values for these samples are shown in Figures 5.3 and 5.4. As can be seen, our theoretical results are in nice agreement with the experiment. In calculating the reflectivity of the samples, we assumed a 5% tolerance which is typical for MBE growth of such structures.

Although MBE has been invented some 20 years ago, some people still consider MBE to be more art than science. Figure 5.5 is a typical proof of this statement. The figure compares the selectivity measurements of two different samples obtained from different growers. Although both wafers were asked to be grown for the epilayer design of RCE1 (Figure 4.9), the resulting characteristics were completely different. The wafer obtained from Iowa State University had reasonable characteristics, while the wafer obtained from University of Virginia

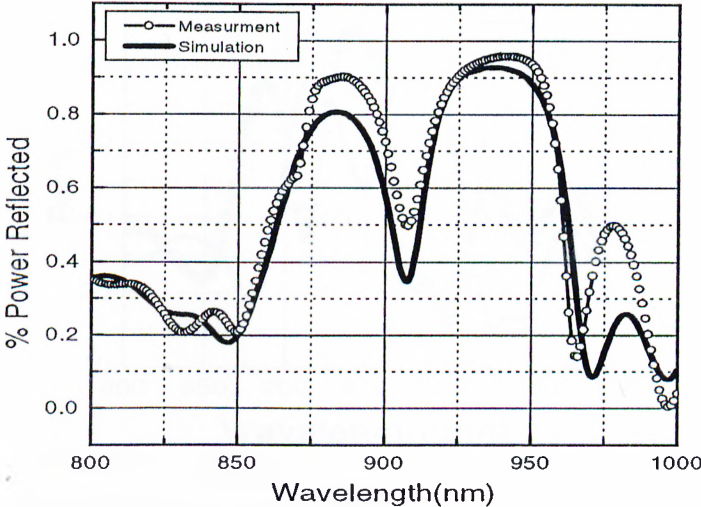


Figure 5.3: Simulated and measured reflectivity of RCE1.

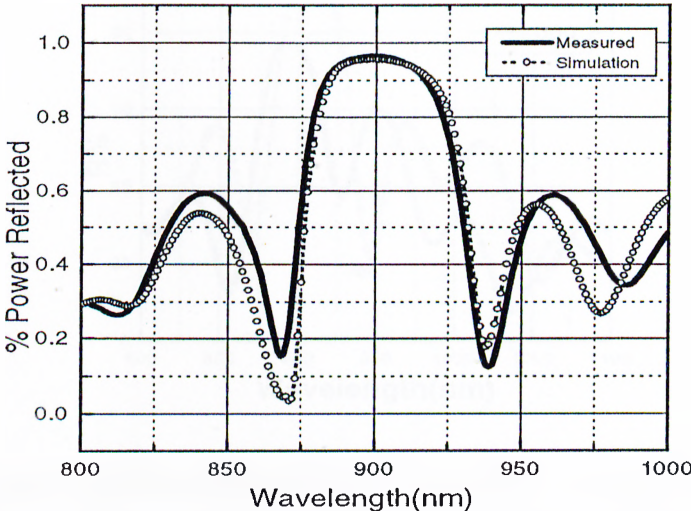


Figure 5.4: Simulated and measured reflectivity of RCE2.

showed resonance at 950 nm instead of the expected 920 nm.

To investigate the effect of etching (shortening the cavity length), RCE2

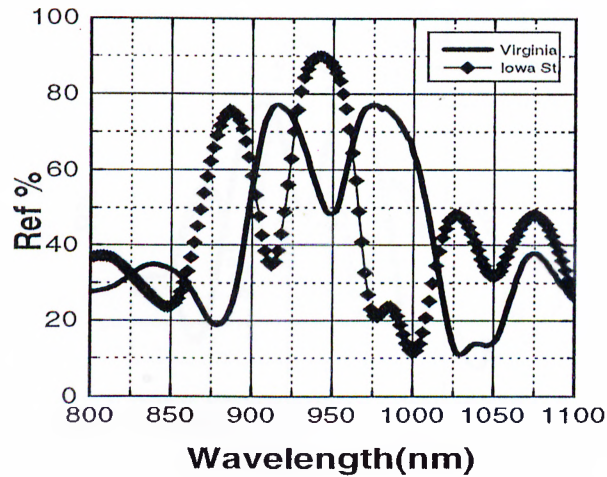


Figure 5.5: Reflectivities of two RCE1 structures grown in two different MBE facilities. The peaks are 35nm apart from each other.

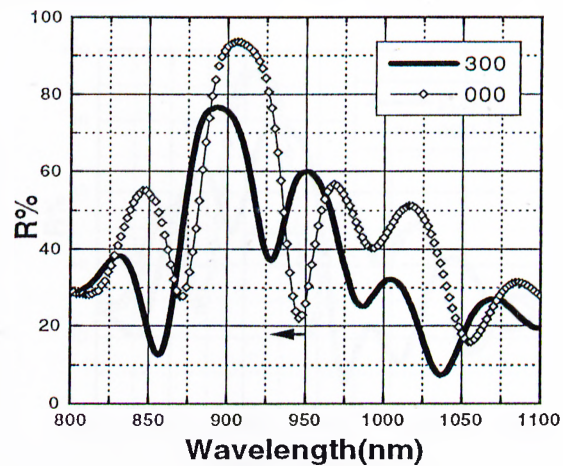


Figure 5.6: Measured reflectivity of 300Å etched RCE2 sample with the reflectivity of unetched RCE2. The resonance wavelength of the etched RCE2 is 925 nm while the original is 945 nm. The direction of wavelength shift is shown by an arrow.

sample was etched 300Å, 600Å, and 900Å. The measured reflectivities for these samples are shown in Figures 5.6, 5.7 and 5.8. As expected, the shortening of the cavity results in a down shift of the reflectivity spectra. For each Å of

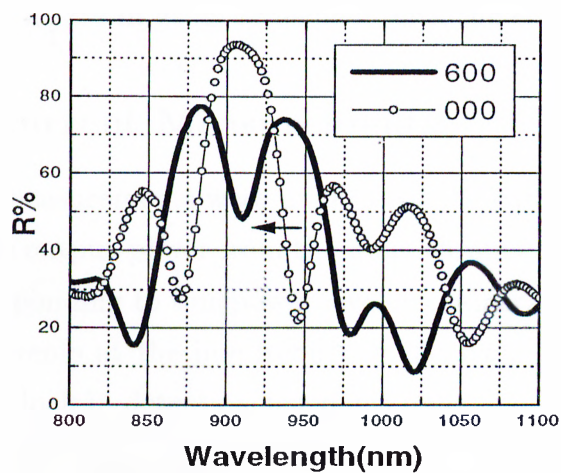


Figure 5.7: Measured reflectivity of 600Å etched RCE2 sample and the unetched RCE2. The resonance of the etched RCE2 is 906 nm. The direction of wavelength shift is shown by an arrow.

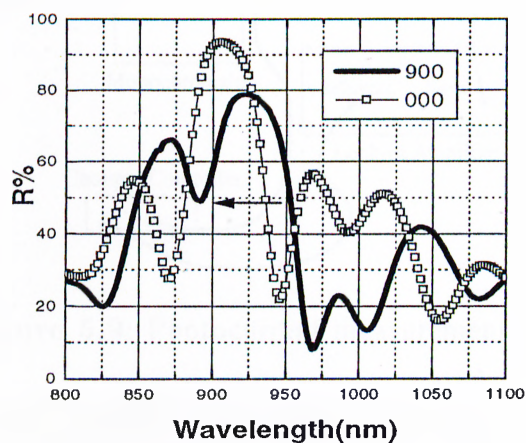


Figure 5.8: Measured reflectivity of 900Å etched RCE2 sample and the unetched RCE2. The peak of the etched RCE2 moved to 892 nm. The direction of wavelength shift is shown by an arrow.

etching, the resonance wavelength uniformly down shifted 0.65\AA . The simulation also predicted similar shifts. First 300\AA etching brought down the resonance peak from 945 nm to 925 nm, second 300\AA etch reduced it to a value of 906

nm and finally we reached 885 nm with another 300\AA etching. The simulated resonance wavelengths are in good agreement with the experimental results.

5.1.2 Photocurrent Measurements

The photocurrent measurements were made with the experimental setup shown in Figure 5.9.³² The output power from the monochromator is around $3\mu\text{W}$. The photocurrent corresponding to this power level is comparable to the dark current and other noise currents at the line frequency (50 Hz). To be able to measure the photocurrent, a lock-in detection scheme is used.

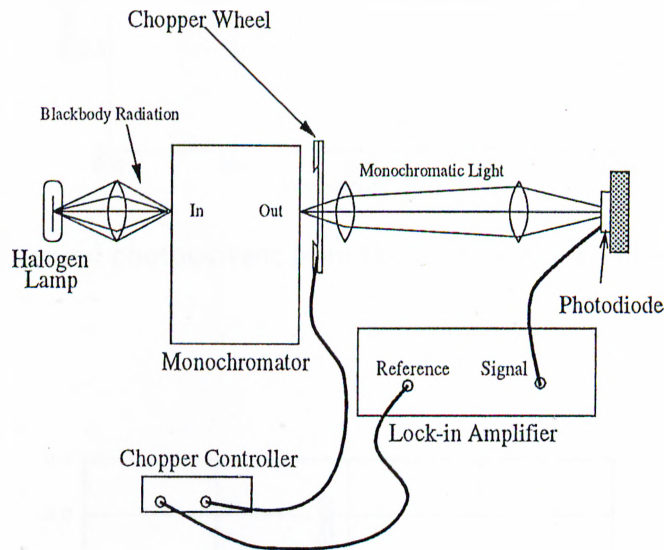


Figure 5.9: Photocurrent measurement setup.

We used the largest diodes on the mask which have an area $250\mu\text{m} \times 250\mu\text{m}$ to measure the photocurrent. Figures 5.10, 5.12 and 5.14 show the measured photoresponses of the devices fabricated using RCE1, RCE2 and 320\AA etched RCE2 samples. RCE1 has a peak quantum efficiency at 894 nm in good agreement with the simulation resonance wavelength. RCE2 was designed for bottom illumination and thus the quantum efficiency, when illuminated from the top, found to be of lower magnitude than it should be when it is illuminated from the bottom surface. The resonant wavelengths are exactly at the values predicted by

simulation, i.e at 925 nm. In order to down shift the resonance wavelength we etched 320\AA from the top surface of the structure and found the peak at 898 nm. All three simulations for quantum efficiencies are shown respectively in Figures 5.11, 5.13 and 5.15.

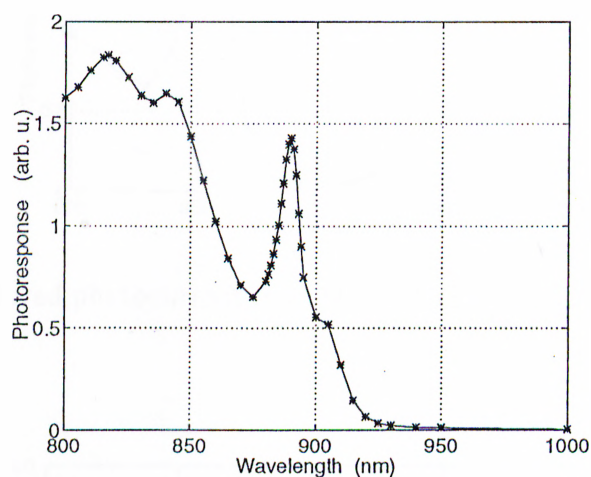


Figure 5.10: Measured photocurrent from the RCE1 sample. The peak wavelength is 894nm.

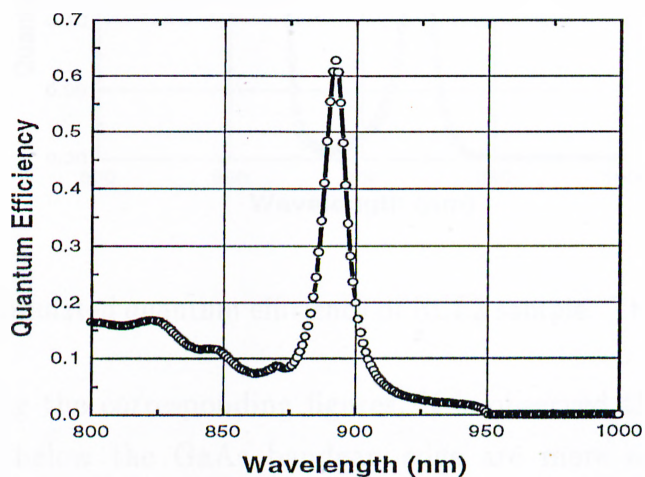


Figure 5.11: Simulated quantum efficiency of RCE1 sample. The peak is at 896 nm.

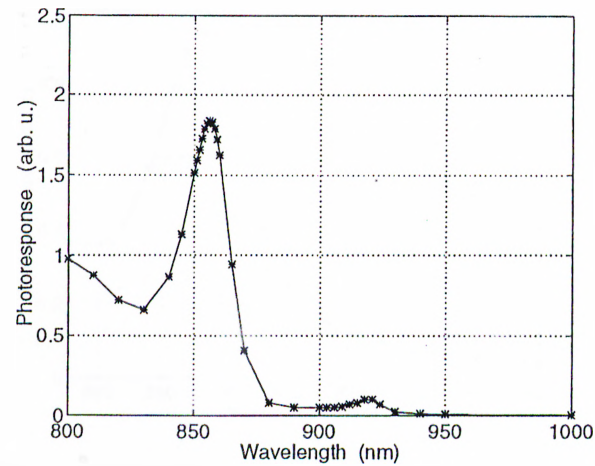


Figure 5.12: Measured photocurrent from the RCE2 sample. The peak wavelength is 925 nm.

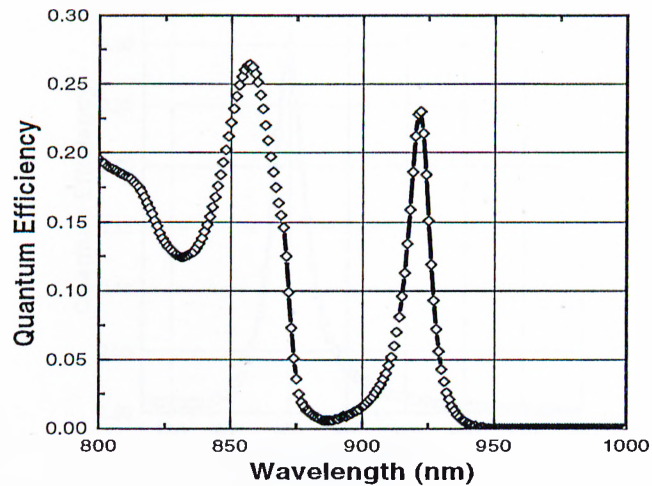


Figure 5.13: Simulated quantum efficiency of RCE2 sample. The peak is at 925nm.

By comparing the corresponding figures, it is observed that the absorption peaks that are below the GaAs bandgap edge are more enhanced than the simulations predict. This is attributed to two reasons. First, the light is focused to an area that is about 20 times larger than the area of the diode. This causes electron-hole generation in regions other than the depletion region. As an

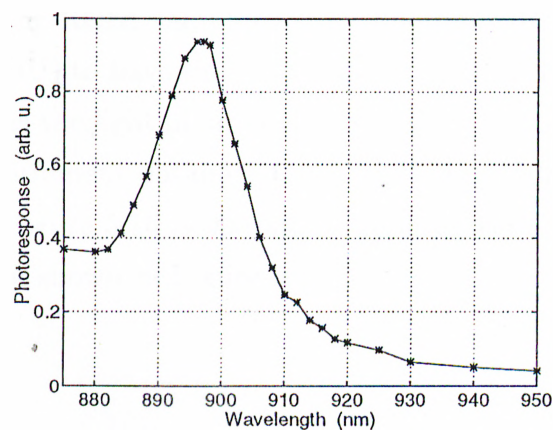


Figure 5.14: Measured photocurrent from the RCE2 320Å etched sample. The peak wavelength is 900 nm.

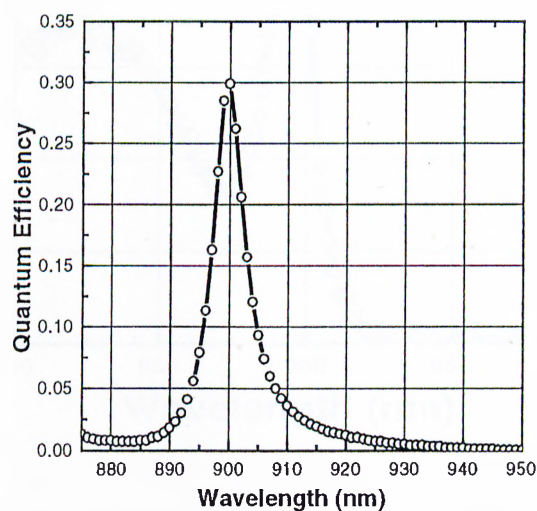


Figure 5.15: Simulated quantum efficiency of RCE2 320Å etched sample. The peak is at 900 nm.

example, it was observed that illumination of the bias resistor of the photodiode circuit caused photocurrent to flow. This photocurrent is ~ 2 - 3 times greater than the actual photocurrent that is typically measured from the same circuit. Another possible reason for the discrepancy between experiment and theory could be a lower absorption coefficient for InGaAs than expected.

We sent one of our RCE1 samples to the Photonics Research Laboratory of Boston University (BU) to have the photocurrent measurements done by using a setup which can focus the light in an area of $85\mu m \times 85\mu m$. Figure 5.16 shows the photoresponse measurement obtained from a $150\mu m \times 150\mu m$ photodiode. The absorption peak in Figure 5.16 is 900 nm in good agreement with the predicted absorption of 900 nm shown in Figure 5.11.

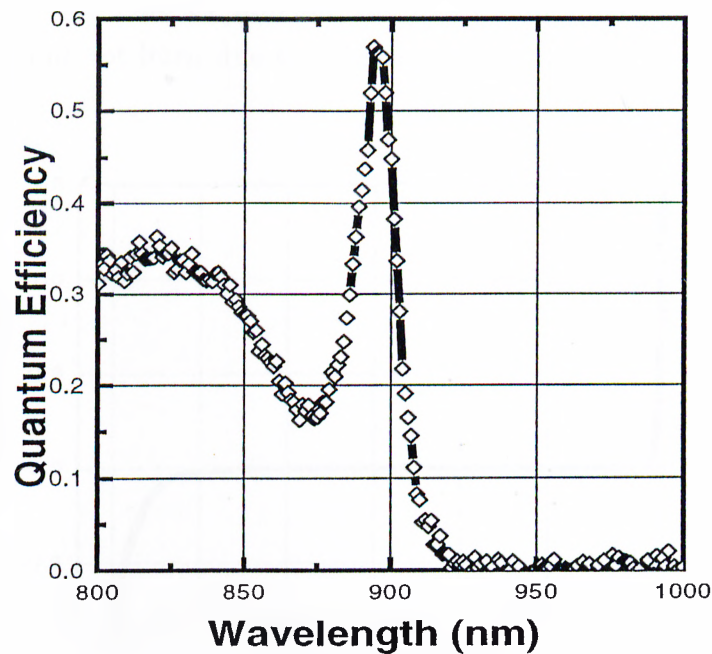


Figure 5.16: Quantum efficiency measurements of RCE1 diodes done at BU. The peak is at 900 nm.

From the measurement done at Bilkent setup, the quantum efficiency for the resonance wavelengths are found to be 0.31 at $\lambda = 889\text{nm}$ for RCE1 sample and 0.38 at $\lambda = 856\text{nm}$ for RCE2 sample. The quantum efficiency was found to be 1.5 times greater than predicted for RCE2 (at $\lambda = 856\text{nm}$) and half of the value that was predicted for RCE1 at ($\lambda = 889\text{nm}$). The resonance wavelengths were, on the other hand, within 2-3nm of predicted values.

5.2 I-V Characterization

We obtained the voltage, current dependence of the photodiodes by using an HP4142B semiconductor parameter analyzer. We first checked the existence of a Schottky diode like characteristic without exceeding ± 1 bias voltage. Then, we increased the reverse bias voltage to measure the value of reverse breakdown. For small diodes the breakdown voltage was as large as -12V , while for bigger diodes such as ($250\mu\text{m} \times 250\mu\text{m}$) the typical breakdown voltage was around -6V . All the measurements were done by limiting the maximum current value to 10mA , so that diodes would not burn due to excess current.

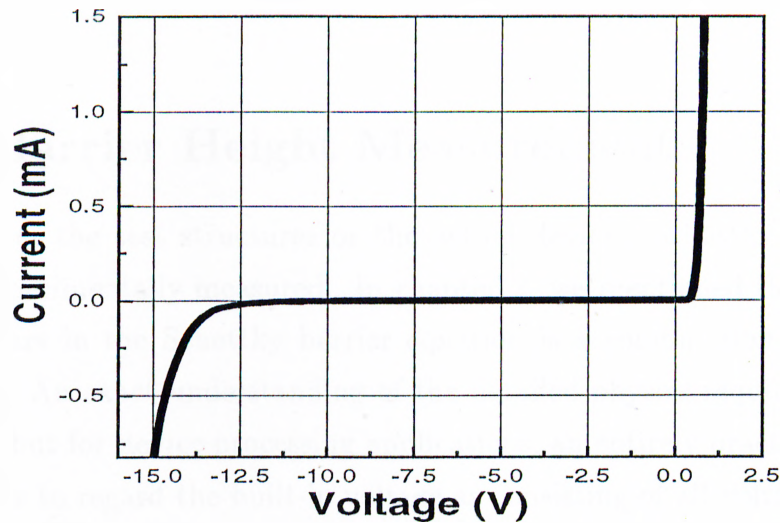


Figure 5.17: I-V characteristics of a small area photodiode.

We calculated that a bias voltage of 5.8 Volts was necessary to deplete the whole depletion region. This means that we could achieve total depletion before reaching the breakdown voltage. Figure 5.17 shows typical I-V curve of a small diode with low leakage and dark current. For an RCE2 diode with an area of $250\mu\text{m} \times 250\mu\text{m}$, the dark current was $0.364\text{mA}/\text{cm}^2$ whereas, a much smaller diode like one with diameter of $30\mu\text{m}$ showed a much higher value of $15.5\text{mA}/\text{cm}^2$.

The detectivity, D^* is defined as the signal-to-noise ratio normalized per unit area per unit noise bandwidth. It is given by,

$$D^* = \frac{\eta \lambda (q/J_o)^{\frac{1}{2}}}{2hc} \text{cmHz}^{\frac{1}{2}}\text{W}^{-1} \quad (5.1)$$

where J_o is the dark current density, η is the quantum efficiency and λ is the peak wavelength.

We calculated the detectivity, D^* of the diodes at -1.0V using Equation 5.1. It was found to be $1.40 \times 10^{12} \text{cmHz}^{1/2}\text{W}^{-1}$ for a $250\mu\text{m} \times 250\mu\text{m}$ diode, while the value is $6.83 \times 10^{10} \text{cmHz}^{1/2}\text{W}^{-1}$ for a $30\mu\text{m}$ diameter diode.

The specific contact resistance r_c of the ohmic contact was also measured. It varied from 3 to $6 \times 10^{-6} \Omega - \text{cm}^2$ which is a reasonably good value for high speed devices.

5.3 Barrier Height Measurement

Using either the test structures or the actual devices, Schottky barrier height can be experimentally measured. In chapter 2, we mentioned that the voltage that appears in the Schottky barrier equation is a combination of V_{bi} , $V_{applied}$ and kT/q . An exact understanding of the detailed physics requires inclusion of all terms, but for device processing applications, an entirely practical and useful approach is to regard the built-in voltage as consisting of all voltage component except $V_{applied}$. Out of four methods used to measure the Schottky barrier height, we have chosen current-voltage method because of its simplicity. To apply this method, we can express the Equation 2.7 as

$$\ln(J) = \ln(J_s) + \frac{qV}{nK_B T} \quad (5.2)$$

$$J_s = A^* T^2 \exp(-q\phi_b/kT) \quad (5.3)$$

where $A^* = 4\pi m_e q K_B^2 / h^3 = 120 \text{Acm}^{-2}\text{K}^{-2}$.

Therefore, a plot of $\ln(J)$ as a function of V should result in straight line having slope q/nkT and intercept $\ln(J_s)$. Using the value of the intercept point J_s can be calculated and the barrier height can be found to be

$$\Phi_b = (kT/q) \ln(A^*T^2/J_s) \quad (5.4)$$

We found the barrier height to be 0.82 eV for 200Å of gold Schottky barrier. Previously, in order to enhance adhesion, 50Å Ti was used below the Au layer in the Schottky metal. We found a 0.62 eV barrier height for this metalization. The former data is pretty near to the theoretical value, while the latter could not be verified with any literature value as no one has reported a similar Schottky metalization. We later stopped using Ti for metalization, as it causes degradation in the Schottky diode quality.

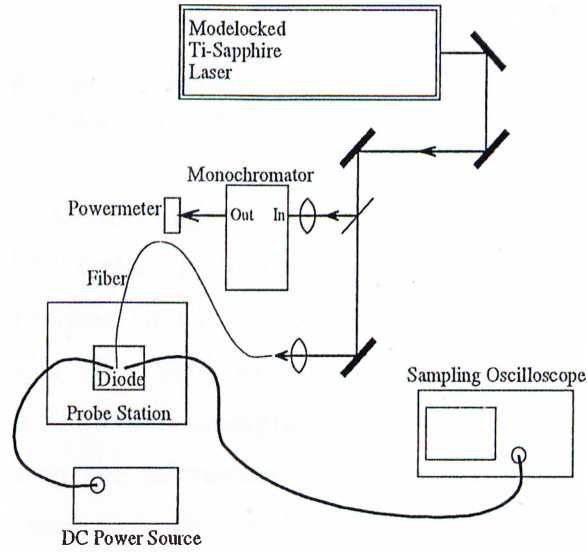


Figure 5.18: High speed measurement setup.

5.4 High Speed Measurements

Previously we mentioned that out of the two samples investigated, RCE1 found to have very low or almost no doping concentrations at the N^+ region (probably due to an error during the growth process). This resulted in a very high contact resistance in the ohmic contacts. In fact, the diodes we fabricated using RCE1 was back to back two Schottky contacts that were used for photoresponse

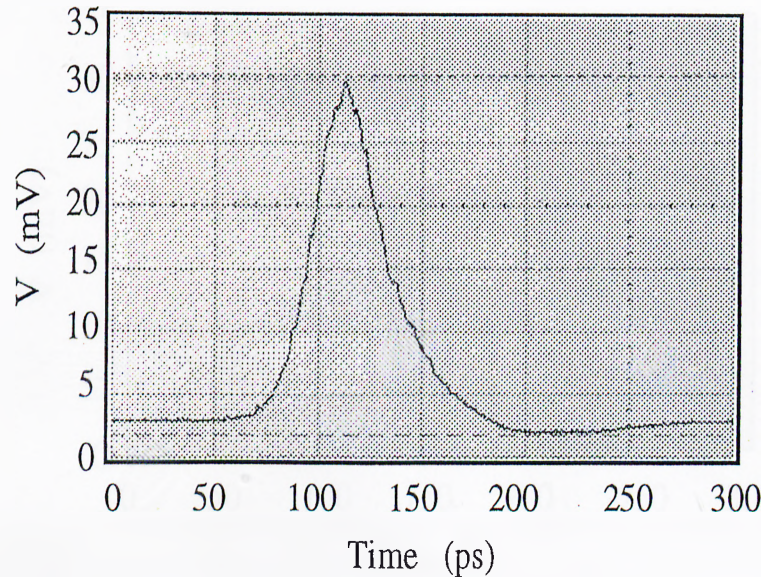


Figure 5.19: High speed measurement of an RCE2 diode with an area of $20\mu\text{m} \times 30\mu\text{m}$. At $\lambda = 850\text{nm}$, FWHM is 35 ps.

measurements only. All the high speed measurements were done using diodes fabricated on the RCE2 wafer. The measurement setup is shown in Figure 5.18.³² Femtosecond optical pulses, that have 120 fsec duration, from the the Ti:Sapphire laser (Coherent Model Mira 900) were first coupled to the fiber using a 20X microscope objective. The light emerging from the fiber was brought close to the surface of the diode on the microwave probe station using a translation stage. The detected pulses were than observed with a sampling oscilloscope (HP Model HP54120B).

The Figures 5.19, 5.20 and 5.21 show oscilloscope traces for various measurements. Figure 5.19 shows a pulse obtained from an RCE2 diode with an area of $20\mu\text{m} \times 30\mu\text{m}$ at zero bias. This pulse has a FWHM of 35 ps which corresponds to a 3-dB bandwidth of 11.5 GHz. The measurement was made at $\lambda = 850\text{ nm}$. Figure 5.20 shows similar pulse width obtained from an RCE2 diode with an area of $7\mu\text{m} \times 7\mu\text{m}$ at $\lambda = 850\text{ nm}$. The pulse in Figure 5.21 is obtained from a $7\mu\text{m} \times 14\mu\text{m}$ diode under zero bias on the 300\AA etched RCE2 sample and it also has a FWHM of 35 ps.

The bandwidth of the measurement setup was measured to be 12GHz. As a

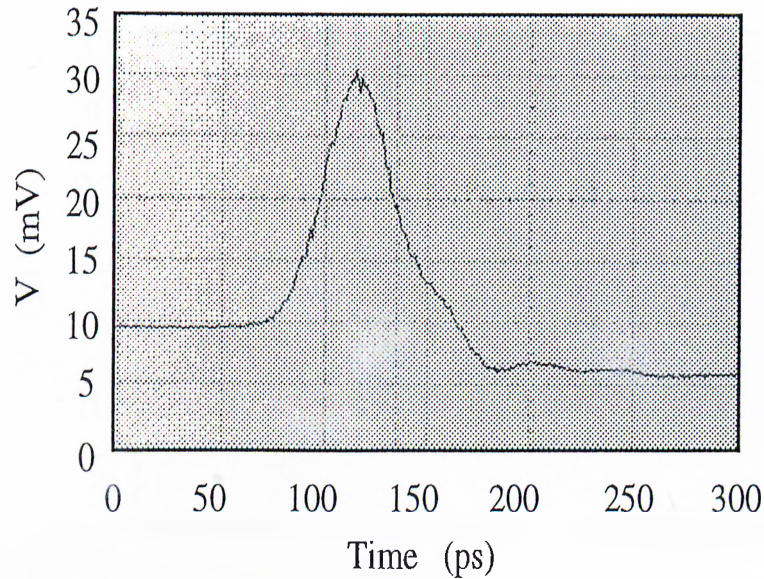


Figure 5.20: High speed measurement of an RCE2 diode with an area of $7\mu\text{m} \times 7\mu\text{m}$. At $\lambda = 850\text{ nm}$, FWHM is 35 ps.

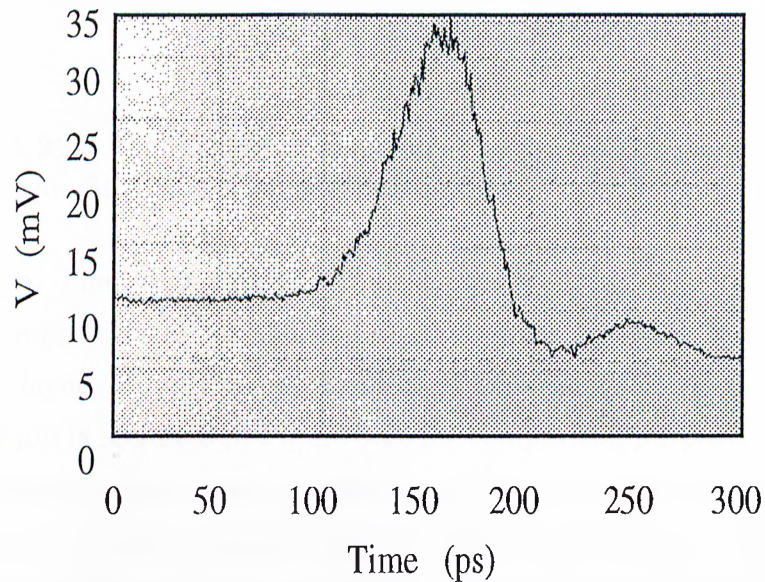


Figure 5.21: High speed measurement of a 320\AA etched RCE2 diode with an area of $7\mu\text{m} \times 14\mu\text{m}$. At $\lambda = 900\text{ nm}$, FWHM is 45 ps.

result, we can conclude that our measurements were limited by the setup. The Figures 5.21 and 5.22 show high speed measurements above GaAs band edge at zero bias. It is observed that, the width of the pulse has increased to 45 ps at

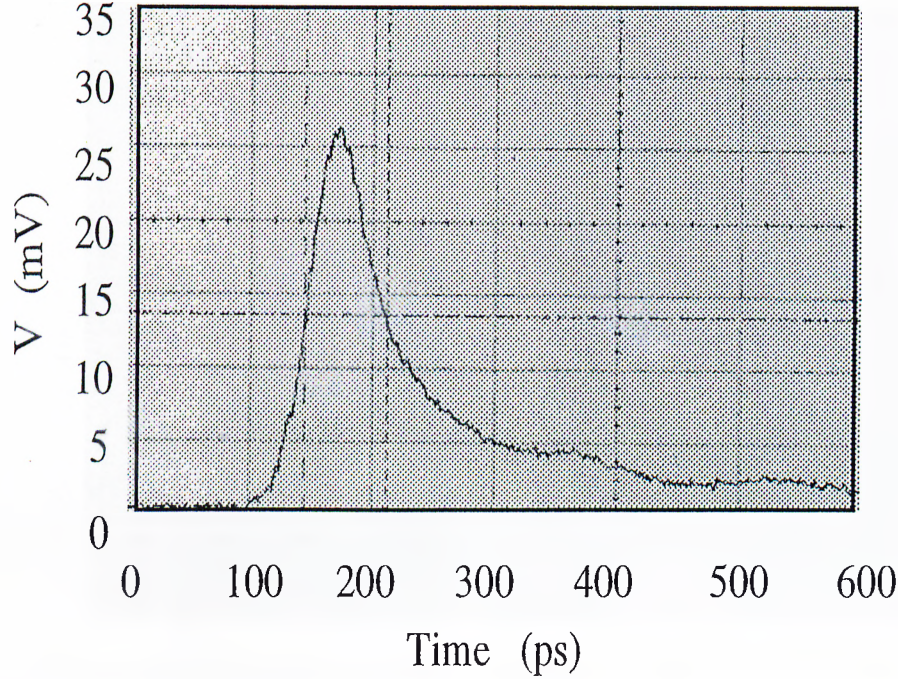


Figure 5.22: High speed measurement of an RCE1 diode with an area of $20\mu\text{m} \times 30\mu\text{m}$. At $\lambda = 890\text{ nm}$, FWHM is 68 ps.

$\lambda = 900\text{nm}$. The reasons for this could be the trapping of carriers at the InGaAs-GaAs heterointerfaces, or the fact that we were not able to deplete the entire depletion layer. Finally, a pulse obtained from an RCE1 diode with an area of $20\mu\text{m} \times 30\mu\text{m}$ is included in Figure 5.22 for comparison purposes. The wavelength of the excitation pulse was $\lambda = 890\text{ nm}$. Since this device did not have a good ohmic contact, current mechanisms other than drift (since a high electric field can not exist in this device) could be dominating. For this diode a pulse with FWHM of 68ps was observed.

We sent samples from all the categories to have the high speed measurements done at the Photonic Research Laboratory at Boston University. Some preliminary results were reported which indicated that the FWHM might go down to values lower than 30 ps. In Figure 5.24 we show the high speed measurement results of a RCE2 diode with an area of $7\mu\text{m} \times 7\mu\text{m}$ at $\lambda = 900\text{ nm}$. The pulse

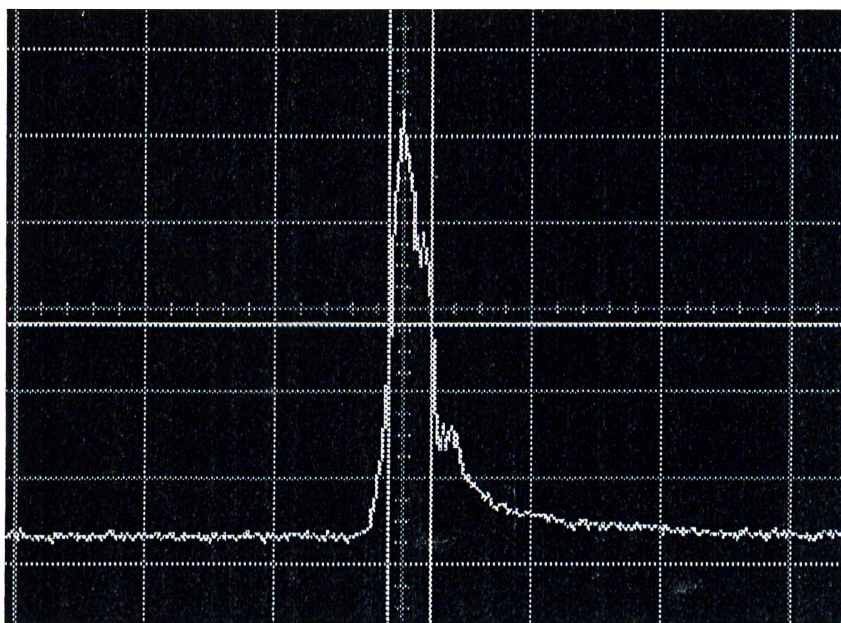


Figure 5.23: High speed measurement of an RCE2 diode with an area of $7\mu\text{m} \times 7\mu\text{m}$. At $\lambda = 900\text{nm}$, FWHM is 30 ps.

has a FWHM of 30 ps which corresponds to a 3-dB bandwidth of 14 GHz. We expect the value to rise up to 30 GHz when the measurements are optimized.

Chapter 6

Conclusion

In this thesis, we presented our efforts in design, fabrication and characterization of a resonant cavity enhanced photodiode with a thin InGaAs absorbing layer. Simulations were done³² for both top and bottom illuminated photodetectors. All the parameters of the resonant microcavity were optimized to enhance the quantum efficiencies of the photodiode at the resonance wavelength which was chosen to be 900 nm. The maximum peak quantum efficiency of the top illuminated device (RCE1) was calculated to be 0.72, while it was 0.80 for the bottom illuminated (RCE2) device. Although optimized for bottom illumination, RCE2 was illuminated from the top surface and the simulated quantum efficiency for this case was 0.22.

The results of our reflectivity measurements for both RCE1 and RCE2 were in good agreement with the simulations. The resonance wavelength of RCE2 was found to be at 945 nm when illuminated from the top surface and it was reduced to 920 nm by etching 320Å from the surface of the microcavity. When diodes were fabricated, this resonance wavelength shifted to 900 nm because of the presence of the 200 Å Au Schottky metal layer. This cavity resonance wavelength tuning process, accurately supported by the simulation, was applied several times to down shift the peak wavelength of the RCE2 wafer. Later, photodiodes were fabricated using these samples and the spectral measurement of photoresponse of the devices were measured. The resultant peaks of the photocurrent were found

to be close to our expected wavelengths. In a way, we have developed an efficient method for overcoming the problems of possible thickness deviations that result from the growth process.

The quantum efficiency measurements done on our samples clearly revealed the resonant nature of our design for both structures. We were able to measure an efficiency of 55% at design wavelength of 900 nm. The I-V characteristics of the diodes were also of very high quality. The reverse bias breakdown was at -12V for the small area diodes. The dark current was at considerably low levels and the detectivity of the devices was relatively high.

Although limited by the performance of the existing high-speed measurement set-up, the results clearly proved the high speed nature of our devices. Pulses of wavelengths shorter than GaAs bandgap wavelength (880 nm) were detected faster (35 ps) while in the case of longer wavelengths, the response was slower (45 ps). The preliminary results from Boston, which is 30 ps, is very encouraging and we hope to receive better results when the setup is optimized. Even the high speed results found at Bilkent can be stated as the best results for any Schottky barrier photodiode ever reported.

We plan to utilize similar methods of increasing the efficiencies by embedding a microcavity and design photodiodes at longer wavelengths suitable for modern telecommunication systems. Schottky photodiodes consisting of $\text{In}_{0.53}\text{Ga}_{0.47}\text{As}$ in the active region can be sensitive out to wavelengths as long as $1.55 \mu\text{m}$. InGaAs is lattice matched to InP and is well known for its inherent higher mobilities and saturation velocities. We also plan to design diodes to operate at 840 nm using GaAs as active material and AlAs/ $\text{Al}_{0.1}\text{Ga}_{0.9}\text{As}$ as DBR mirror. Both AlAs and $\text{Al}_{0.1}\text{Ga}_{0.9}\text{As}$ are transparent above 800 nm.

We stated that RCE2 was illuminated from the top surface although it was designed for bottom illumination. In the immediate future, we will try to develop the processes for preparing bottom illuminated samples which were expected to yield better efficiencies than top illuminated devices. By designing better and more suitable structures for photoresponse and high speed measurements, we plan to further improve the quality of our characterization processes.

Bibliography

- [1] H. C. Huang, "A novel millimeter-wave gallium arsenide beam-lead mixer diode with cutoff frequency of 2 THz," *Canadian Journal of Phys.* **69**, 480 (1991).
- [2] R. U. Titz, "Investigation of GaAs schottky barrier photodiode in the THz range," *J. of Infrared and Millimeter Waves*, **11**, 809 (1990).
- [3] A. Raisanen, "Capability of Schottky-diode multipliers as local oscillators at 1 THz," *Microwave and Optical Tech Lett.* **4**, 29 (1991).
- [4] S.Y. Wang, D. M. Bloom, "1-GHz bandwidth planar GaAs Schottky photodiode," *Electron. Lett.* **19**, 554 (1983).
- [5] D. G. Parker, P.G. Say, A.M. Hanson, and W. Sibbett, "110 GHz high efficiency photodiodes fabricated from Indium tin oxide/GaAs," *Electron. Lett.* **22**, 1266 (1989).
- [6] I-Hsing Tan, Chi Kuang Sun, Kirk S. Giboney, John E. Bowers, Evelyn L. Hu, B. I. Miller, and R. J. Capik, "120 GHz long-wavelength lowcapacitance photodetector with an air-bridged coplanar metal wave-guide," *Photonic Technology Lett.* **7**, 1477 (1995).
- [7] E. Özbay, K. D. Li and D.M bloom, "2.0 psec, 150GHz, monolithic photodiode and all-electronic sampler" *IEEE Photon Tech. Lett.* **3**, 570 (1991).

- [8] K. D. Li, E. Özbay, J. A. Sheridan, and D.M. Bloom, "1.8 psec, 200 GHz GaAs photodiode and all-electronic sampler" Proceed, of Conference on lasers and Electro Optics (CLEO), May 1991.
- [9] A. Chin and T. Y. Chang, "Multilayer reflectors by molecular beam epitaxy for resonance enhanced absorption in thin high speed detectors," *J. Vac. Sci. Technol.* **B8**, 339 (1990)
- [10] B. Sverdlov, A. Botchkarev, N. Teraguchi, A. Salvador and H. Morkoc, *Electron. Letters*, **29**, 1019 (1993).
- [11] Y.G. Wey, M. Kamegawa, A. Mar, K.J. Williams, K. Giboney, D. L. Crawford, J. E. Bowers and M. J. Rodwell, "Hybrid integration of an InGaAs/InP PIN photodiode with an ultrafast sampling circuit," *Optic Fiber Conference*, **PD12-4** (1991).
- [12] F. Mansoor, S. K. Haywood, N. J. Mason, R. J. Nicholas, P.J. Walker, R. Grey, and J. Hill, "RCE photodetectors based on Ga(In)Sb for gas-sensing applications," *Semicond. Sci. and Technol.* **10**, 1017 (1995).
- [13] C. Y. Chang, F. Kai, "GaAs High Speed Devices" John Wiley and Sons, New York, 284 (1994).
- [14] R. William, "Modern GaAs Processing Methods" Artech House, Boston, 243 (1990).
- [15] A. Padovani, and R. Stratton, *Solid State Electron.* **9**, 695 (1966).
- [16] S. S. Li, "Semiconductor Physical Electronics," Plenum Press, New York, 344 (1993).
- [17] G. Lucovosky, R. F. Schwrz, and R. B. Emmons, "Transit-time considerations in p-i-n diodes," *J. Appl. Phys.* **35**, 622 (1964).
- [18] R. William, "Modern GaAs Processing Methods" Artech House, Boston, 279 (1990).

- [19] T. Batchelder and J. Piatt, *Solid St. Technol.* **26**, 211 (1983).
- [20] S. Adachi and K. Oe, *J. Electrochem. Soc.* **130**, 2427 (1983).
- [21] D. Shaw, *J. Electrochem. Soc.* **128**, 874 (1981).
- [22] E. Özbay, "Breaking world records in high speed microelectronics," Stanford University Ph.D. thesis, February 1992.
- [23] A. Chin, Y. Chang , "Multilayer reflectors by molecular beam epitaxy for resonance enhanced absorption in thin high speed detectors," *J. Vac. Sci. Technol.* **B8**, 339 (1990).
- [24] M. S. Ünlü, S. Strite, "Resonant cavity enhanced photonic devices," *J. Appl. Phys.* **78**, 1 (1995).
- [25] R. Kuchibolta, A. Spinivason, J. Campbell, C. Lei, D. Deppe, Y. He, and B. Streetmen, "Low-voltage high-gain resonant cavity avalanche photodiode," *IEEE Photonic Technology Lett.* **3**, 354 (1991).
- [26] K. Xie, J. Zhao, Y. Shi, H. Lee and G. Olsen, "Resonant cavity enhanced GaInAsSb-AlAsSb photodetector grown by MBE for mid-IR applications," *IEEE Phot. Tech. Lett.* **8**, 5 667 (1996).
- [27] M. Gökkavaş, "Design and characterization of RCE photodetectors," Bilkent University M.S. Thesis, 35 (1996).
- [28] T. Yen-Chang, S. Sheng, H. Pin, "A GaAs photodiode with high quantum efficiency-bandwidth product by using multilayer reflector," *IEEE Trans. Elec. Dev.* **40**, 348 (1992).
- [29] S. Datta, "Quantum Phenomena," New York: Addison-Wesley, (1989).
- [30] C. Schneider, "Schottky barrier photodiodes with antireflection coating," *Bell. Syst. Tech. J.* **45**, 1611 (1966).

- [31] E. D. Palik, "Handbook of optical constants of solids" Orlando: Academic Press, (1985).
- [32] M. Gökkaş, "Design and characterization of RCE photodetectors," Bilkent University M.S. Thesis, 49 (1996).